

# Glueball Properties at Finite Temperature in SU(3) Anisotropic Lattice QCD

Noriyoshi Ishii

*The Institute of Physical and Chemical Research (RIKEN),  
2-1 Hirosawa, Wako, Saitama 351-0198, Japan*

Hideo Suganuma

*Faculty of Science, Tokyo Institute of Technology,  
2-12-1 Ohkayama, Meguro, Tokyo 152-8552, Japan*

Hideo Matsufuru

*Yukawa Institute for Theoretical Physics, Kyoto University,  
Kitashirakawa-Oiwake, Sakyo, Kyoto 606-8502, Japan*

The thermal properties of the glueballs are studied using SU(3) anisotropic lattice QCD with  $\beta_{\text{lat}} = 6.25$ , the renormalized anisotropy  $\xi \equiv a_s/a_t = 4$  over the lattice of the size  $20^3 \times N_t$  with  $N_t = 24, 26, 28, 30, 33, 34, 35, 36, 37, 38, 40, 43, 45, 50, 72$  at the quenched level. To construct a suitable operator for the lowest-state glueball on the lattice, we adopt the smearing method, providing an illustration of its physical meaning in terms of the operator size. First, we construct the temporal correlators  $G(t)$  for the lowest  $0^{++}$  and  $2^{++}$  glueballs, using more than 5,500 gauge configurations at each temperature  $T$ . We then perform the pole-mass measurement of the thermal glueballs from  $G(t)$ . For the lowest  $0^{++}$  glueball, we observe a significant pole-mass reduction of about 300 MeV in the vicinity of  $T_c$  or  $m_G(T \simeq T_c) \simeq 0.8m_G(T \sim 0)$ , while its size remains almost unchanged as  $\rho(T) \simeq 0.4$  fm. Finally, for completeness, as an attempt to take into account the effect of thermal width  $\Gamma(T)$  at finite temperature, we perform a more general new analysis of  $G(t)$  based on its spectral representation. As an ansatz to the spectral function  $\rho(\omega)$ , we adopt the Breit-Wigner form, and perform the best-fit analysis of the temporal correlator as a straightforward extension to the standard pole-mass analysis. The result indicates a significant broadening of the peak as  $\Gamma(T) \sim 300$  MeV as well as rather modest reduction of the peak center of about 100 MeV near  $T_c$  for the lowest  $0^{++}$  glueball. The temporal correlators of the color-singlet modes corresponding to these glueballs above  $T_c$  are also investigated.

PACS numbers: 12.38.Gc, 12.39.Mk, 12.38.Mh, 11.15.Ha

## I. INTRODUCTION

QCD at finite temperature is one of the most interesting subjects in the quark hadron physics [1, 2, 3]. At low temperature, quarks and gluons are confined in the color-singlet objects, hadrons, due to the nonperturbative effect of the strong interactions among them. With the increasing temperature, these interactions diminish due to the asymptotic freedom, which is expected to lead to liberation of quarks and gluons above a critical temperature  $T_c$ , forming the new phase, i.e., the quark-gluon plasma (QGP) phase.

At present, we are in front of the experimental possibility to create the QGP phase in the RHIC project at Brookhaven National Laboratory. Hence, much progress is desired in the theoretical understanding of QCD at finite temperature. To study QCD at finite temperature and to understand the QCD phase transition, the effective models and the lattice QCD Monte Carlo simulation provide useful and complementary approaches. While the effective models offer their own insights into the physical phenomena and often provide analytical methods to estimate related physical quantities, the lattice QCD simulation provides a model-independent method of calculating physical quantities directly based on QCD.

The SU(3) lattice QCD at the quenched level indicates the deconfinement phase transition of the weak first order at the critical temperature  $T_c \simeq 260$  MeV [4], and simulations with dynamical quarks show the chiral phase transition at  $T_c = 173(8)$  MeV for  $N_f = 2$  and  $T_c = 154(8)$  MeV for  $N_f = 3$  in the chiral limit [5].

Above  $T_c$ , most of nonperturbative properties such as color confinement and spontaneous chiral-symmetry breaking disappear. Consequently, quarks and gluons are liberated, and the tremendous changes are expected in the mass spectrum.

Even below  $T_c$ , one is interested in the hadronic mass shift [2, 6, 7], because it can be one of the most important pre-critical phenomena of the QCD phase transition at finite temperature (and also at finite density). In this respect, from the experimental side for instance, CERES Collaboration [8] has proposed the high-energy heavy-ion collision data, which may indicate the mass shift of  $\rho$ -meson, and extensive theoretical efforts have been made aiming at understanding of its true implications [9].

The theoretical background to believe in the hadronic mass shift is as follows. As the temperature increases up close to  $T_c$ , the inter-quark potential is known to change significantly [10, 11]. As far as the heavy quarkonia are concerned, for instance  $J/\psi$ , the change of the inter-quark potential may be followed by the changes in the

structures of hadrons, which may lead to significant mass shifts as a consequence [2]. One also expects significant mass shifts of the light hadrons, for instance,  $\sigma$ -meson [6], which is due to the partial chiral restoration.

At finite temperature, due to the absence of the Lorentz invariance, the concept of the “mass” becomes less definitive, and there emerge two distinct concepts of the “screening mass” and the “pole-mass”. The screening mass governs the correlations along the spatial direction, while the pole-mass governs the correlations along the temporal direction. The relation between them is analogous to the relation between the Debye screening mass and the plasma frequency in electro dynamics [12]. Both of these two masses are interesting quantities, which can reflect the important nonperturbative features of QCD. However, we are more interested here in the pole-mass than in the screening mass, because the pole-mass is closely related to the QGP creation experiments and calculations mentioned above. In fact, the pole-mass is expected to be directly observed as the physical mass of the thermal hadrons.

In contrast to the effective model approaches, which have been extensively used to study the thermal properties of hadrons [2, 6], only a few lattice QCD studies have been performed for the pole-mass of thermal hadrons so far [13, 14, 15, 16]. Instead, the screening mass has been extensively studied with the lattice QCD [12, 17, 18, 19] by analyzing the spatial correlations of the hadronic correlators. The reason behind this is the technical difficulty of measuring hadronic two-point correlators in the temporal direction at finite temperature on the lattice. In fact, since the temporal extension of the lattice shrinks as  $1/T$  at high temperature, the pole-mass measurements have to be performed in the limited distance shorter than  $1/(2T)$ , which corresponds to  $N_t/2 = 2-4$  near  $T_c$  in the ordinary isotropic lattice QCD [12].

The severe limitation on the measurement of the temporal correlation can be avoided with an anisotropic lattice where the temporal lattice spacing  $a_t$  is smaller than the spatial one  $a_s$  [20]. On the anisotropic lattice, by taking a small  $a_t$ , it is possible to use efficiently a large number of the temporal lattice points even in the vicinity of  $T_c$ , while the physical temporal extension  $1/T = N_t a_t$  is kept fixed. In this way, the number of available temporal data are largely increased on the anisotropic lattice, and accurate pole-mass measurements from the temporal correlation become possible.

In this paper, we study the glueball properties at finite temperature from the temporal correlation in SU(3) anisotropic lattice QCD. The glueballs are special and interesting hadrons. They belong to a different class of hadrons. Unlike mesons and baryons, which mainly consist of valence quarks and anti-quarks, the glueballs mainly consist of gluons in a color-singlet combination. Their existences are theoretically predicted in QCD as a consequence of the self-interactions among gluons, and numbers of lattice QCD calculations have been performed aiming at investigating the properties of glueballs

[21, 22, 23]. In the real world, the glueballs are expected to mix with the  $q\bar{q}$  mesons due to the presence of the light dynamical quarks. This mixing problem raises a difficulty in distinguishing them from ordinary mesons in full lattice QCD as well as in experiments. Still, enormous experimental efforts have been and are being made in the pursuit of the glueballs in the real world [24]. At present,  $f_0(1500)$  and  $f_0(1710)$  are taken as serious candidates for the  $0^{++}$  glueball, and  $\xi(2230)$  for the  $2^{++}$  glueball, and these glueball candidates are considered to contain substantial fractions of glueball component. In this paper, to avoid this difficulty of identifying the glueball, we adopt quenched lattice QCD as a necessary first step before attempting to include the effect of dynamical quarks in future. It is worth mentioning here that, even without dynamical quarks, quenched lattice QCD reproduces well various masses of hadrons, mesons and baryons, as well as the important nonperturbative quantities such as the string tension and the chiral condensate.

In quenched QCD, the elementary excitations are only glueballs in the confinement phase below the critical temperature  $T_c \simeq 260$  MeV. From the lattice QCD studies at quenched level [21, 22, 23], the lightest physical excitation at zero temperature is known to be the scalar glueball with  $J^{PC} = 0^{++}$  and the mass  $m_G(0^{++}) \simeq 1500-1700$  MeV, and the next lightest one is the tensor glueball with  $J^{PC} = 2^{++}$  and  $m_G(2^{++}) \simeq 2000-2400$  MeV. These light glueballs are expected to play the important role in the thermodynamic properties of quenched QCD below  $T_c$ . Our aim is to understand the thermodynamic properties of quenched QCD below  $T_c$  from the view point of the thermal properties of the lowest-lying  $0^{++}$  and the  $2^{++}$  glueballs.

In our previous paper, only the numerical result of the pole-mass reduction of the  $0^{++}$  glueball at finite temperature was presented [16]. In the present paper, we go into more detail. We reformulate the pole-mass measurement itself from the viewpoint of the spectral representation of the temporal correlator. In addition to the  $0^{++}$  glueball, we also consider the  $2^{++}$  glueball including the deconfinement phase above the critical temperature  $T_c$  as well. Furthermore, based on the spectral representation, we attempt to take into account the effects of the possible appearance of the thermal width of the bound-state peak at finite temperature by proposing the best-fit analysis of the Breit-Wigner type.

The contents are organized as follows. In Sect. II, we begin with a brief review of the spectral representation of the temporal glueball correlator. We then introduce the smearing method as a method to enhance the ground-state contribution in the glueball correlator, and consider the physical meaning of the smearing method. We also give a prescription how to make a rough estimate of the glueball size based on the informations from the temporal glueball correlators with the smearing method. Sect. III is devoted to the brief descriptions of the lattice QCD action, its parameters, the determination of the scale, and the critical temperature  $T_c$  in our anisotropic lat-

tice. In Sect. IV, we construct the temporal glueball correlators based on SU(3) lattice QCD, and perform the pole-mass measurements assuming that the thermal width of the peak in the spectral function is sufficiently narrow. We study the low-lying  $0^{++}$  and  $2^{++}$  glueballs both below and above  $T_c$ . This procedure itself has been widely used in the standard mass measurements of various hadrons in the lattice QCD Monte Carlo calculations at zero temperature. It was also adopted by [13, 14, 16] in the pole-mass measurements of various mesons at finite temperature. The section is closed with the comparison of our results with the related lattice QCD results on the screening masses and the pole masses at finite temperature. In Sect. V, for completeness, we perform a more general new analysis of the temporal correlators of glueballs as an attempt to take into account the effects of the possible appearance of the non-zero thermal width of the bound-state peak at finite temperature. We adopt Breit-Wigner ansatz for the form of the spectral function to extract the center and the thermal width of the ground-state peak through the spectral representation. This procedure itself is a straightforward extension to the procedure adopted in the pole-mass measurements, which seems to be widely applicable to various temporal correlators of thermal hadrons. Sect. VI is devoted to the summary and concluding remarks.

## II. THE SMEARING METHOD IN QUENCHED SU(3) LATTICE QCD

### A. The spectral representation

Using the glueball operator  $\phi_0(t, \vec{x})$ , we consider the temporal correlator of the glueball as

$$G(t) \equiv \langle \phi(t) \phi(0) \rangle, \quad (1)$$

where  $\phi(t)$  is the zero-momentum projected operator defined as

$$\phi(t) \equiv \phi_0(t) - \langle \phi_0 \rangle, \quad \phi_0(t) \equiv \frac{1}{N_s} \sum_{\vec{x}} \phi_0(t, \vec{x}), \quad (2)$$

with  $N_s \equiv N_x N_y N_z$  being the number of sites in the spatial submanifold. The angular bracket  $\langle \cdot \rangle$  denotes the statistical average. The subtraction of the vacuum expectation value is necessary for the  $0^{++}$  glueball. The summation over  $\vec{x}$  is performed for the zero-momentum projection, i.e., the total momentum is set to be zero. The glueball operator  $\phi_0(t, \vec{x})$  has to be properly constructed so as to have a definite spin and parity in the continuum limit. For instance, the  $0^{++}$  and  $2^{++}$  glueball operator are defined as [21, 22, 25, 26]

$$\begin{aligned} \phi_0(t, \vec{x}) &\equiv \text{ReTr} \left( P_{12}(t, \vec{x}) + P_{23}(t, \vec{x}) + P_{31}(t, \vec{x}) \right), \quad (3) \\ \phi_0(t, \vec{x}) &\equiv \text{ReTr} \left( 2P_{12}(t, \vec{x}) - P_{23}(t, \vec{x}) - P_{31}(t, \vec{x}) \right), \end{aligned}$$

respectively, where  $P_{ij}(t, \vec{x})$  denotes the plaquette operator in the  $i$ - $j$  plane.

To consider the spectral representation, we express the temporal correlator  $G(\tau)$  in the canonical operator representation as

$$G(\tau) = Z(\beta)^{-1} \text{tr} \left( e^{-\beta H} \phi(\tau) \phi(0) \right), \quad (4)$$

where  $\beta = 1/T$  denotes the inverse temperature,  $Z(\beta) \equiv \text{tr}(e^{-\beta H})$  the partition function, and  $H$  the Hamiltonian of QCD. The field operator  $\phi(\tau)$  is represented in the imaginary-time Heisenberg picture as  $\phi(\tau) = e^{\tau H} \phi(0) e^{-\tau H}$ . By using the identity  $G(\tau) = G(\beta - \tau)$  for the manifest periodicity, we obtain the spectral representation as

$$\begin{aligned} G(\tau) &= \sum_{n,m} \frac{|\langle n | \phi | m \rangle|^2}{2Z(\beta)} \exp \left( -\beta \frac{E_m + E_n}{2} \right) \quad (5) \\ &\quad \times \cosh \left[ (\tau - \beta/2)(E_n - E_m) \right] \\ &= \int_{-\infty}^{\infty} \frac{d\omega}{2\pi} \frac{\rho(\omega)}{2 \sinh(\beta\omega/2)} \cosh \left( \omega(\beta/2 - \tau) \right), \end{aligned}$$

where  $E_n$  denotes the energy of the  $n$ -th excited state  $|n\rangle$ . In this paper,  $|0\rangle$  denotes the vacuum, and  $|1\rangle$  denotes the lowest glueball state. Here,  $\rho(\omega)$  denotes the spectral function defined as

$$\begin{aligned} \rho(\omega) &\equiv \sum_{n,m} \frac{|\langle n | \phi | m \rangle|^2}{Z(\beta)} e^{-\beta E_m} \quad (6) \\ &\quad \times 2\pi \left( \delta(\omega - E_n + E_m) - \delta(\omega - E_m + E_n) \right). \end{aligned}$$

Note that  $\rho(\omega)$  is positive for positive  $\omega$ , and negative for negative  $\omega$ . Due to the bosonic nature of the glueballs,  $\rho(\omega)$  is odd in  $\omega$ .

The spectral function  $\rho(\omega)$  is the residue of the glueball correlator in the Fourier representation as

$$G(\omega_l) = \int_0^\beta d\tau e^{-i\omega_l \tau} G(\tau) = \int_{-\infty}^{\infty} \frac{d\omega'}{2\pi} \frac{\rho(\omega')}{i\omega_l - \omega'}, \quad (7)$$

where  $\omega_l \equiv \frac{2\pi l}{\beta}$  denotes the Matsubara frequency for bosons. It is also the residue of the retarded and advanced Green functions  $G_R(\omega)$  and  $G_A(\omega)$  as [27]

$$G_{R/A}(\omega) = \int_{-\infty}^{\infty} \frac{d\omega'}{2\pi} \frac{\rho(\omega')}{\omega - \omega' \pm i\epsilon}. \quad (8)$$

(+ for the retarded and - for the advanced Green functions.) Hence, the information of the physical observables such as the mass and the width can be obtained by parameterizing the spectral function  $\rho(\omega)$  properly and by performing the best-fit analysis to the lattice QCD Monte Carlo data of the temporal correlator  $G(t)$  through the spectral representation Eq. (5).

## B. The smearing method

For the study of the low-lying glueballs, it is important to extract the contributions of the low-lying states in lattice QCD Monte Carlo simulations. The smearing method is one of the most popular numerical techniques to enhance the contributions from the low-lying states. Here, we give a brief review of the smearing method in SU(3) lattice QCD in the zero-temperature limit. In this limit  $\beta \equiv 1/T \rightarrow \infty$ , the spectral function  $\rho(\omega)$  and the correlator  $G(t)$  are simply expressed as

$$\rho(\omega) = \sum_n 2\pi A_n \left( \delta(\omega - E_n) - \delta(\omega + E_n) \right), \quad (9)$$

$$\frac{G(t)}{G(0)} = \sum_n C_n \exp(-E_n t),$$

with  $A_n \equiv |\langle n | \phi | 0 \rangle|^2 / Z$  and

$$C_n \equiv \frac{A_n}{\sum_k A_k} = \frac{|\langle n | \phi | 0 \rangle|^2}{\sum_k |\langle k | \phi | 0 \rangle|^2}. \quad (10)$$

Note that  $C_n$  is a non-negative real number with  $0 \leq C_n \leq 1$  with the normalization as  $\sum C_n = 1$ . It will be referred to as the overlap between the state  $\phi|0\rangle$  and the  $n$ -th asymptotic state  $|n\rangle$ .

In general, to measure the ground-state mass from  $G(t)$ , one seeks for the region where contributions from excited states almost die out, leaving only the ground-state component as  $G(t)/G(0) \simeq C_1 \exp(-E_1 t)$ . In this region, one may perform the best-fit analysis with

$$C \exp(-m_G t) \quad (11)$$

to obtain the ground-state mass  $m_G = E_1$  and the ground-state overlap  $C = C_1$ . (Here, as was mentioned in the previous subsection,  $|1\rangle$  denotes the state of the lowest-lying glueball, while  $|0\rangle$  denotes the vacuum state. Because  $\phi(t)$  is the zero-momentum projected operator, defined in Eq. (2),  $E_n$  denotes the mass of the  $n$ -th state.) In principle, such a region always exists for enough large  $t$  in the zero-temperature case. However, in practice, it is difficult to use such large  $t$  in lattice QCD Monte Carlo calculations, since the correlator  $G(t)$  decreases exponentially with  $t$  and becomes so small for the large  $t$  that it is comparable to its statistical error. Hence, to measure the mass of the ground-state, it is essential that the ground-state overlap  $C_1$  should be sufficiently large. In the case of the glueballs in quenched SU(3) lattice QCD, the ground-state overlaps  $C_1$  of the operators given in Eq. (3) are quite small, as long as they are constructed from the simple plaquette operators  $P_{ij}(t, \vec{x})$ . In this case, due to the considerable contributions from excited states, the measured mass with Eq. (11) always behaves as if it were much heavier. The difficulty of this small overlap originates from the fact that the plaquette operator has a smaller ‘‘size’’ of  $O(a)$  than the physical

size of the glueball [28]. This problem becomes severer near the continuum limit. Hence, for the accurate mass measurement, it is necessary to enhance the ground-state contribution by improving the glueball operator. This is achieved by making the operator have approximately the same size as the physical size of the glueball. The smearing method provides an iterative procedure to generate such an extended operators, which is referred to as the smeared operators [21, 26, 28, 29].

The smeared operator is obtained by replacing the original spatial link variables  $U_i(s)$  in the plaquette operators by the associated fat link variables  $U_i^{(n)}(s)$ . Starting from  $U_i^{(0)}(s) \equiv U_i(s)$ , the  $(n+1)$ -th fat link variable  $U_i^{(n+1)}(s) \in \text{SU}(3)$  is defined iteratively from  $U_i^{(n)}(s)$  so as to maximize

$$\text{ReTr} \left( U_i^{(n+1)}(s) V_i^{(n)\dagger}(s) \right), \quad (12)$$

with

$$V_i^{(n)}(s) \equiv \alpha U_i^{(n)}(s) \quad (13)$$

$$+ \sum_{\pm, j \neq i} U_{\pm j}^{(n)}(s) U_i^{(n)}(s \pm \hat{j}) U_{\pm j}^{(n)\dagger}(s + \hat{i}),$$

where  $U_{-\mu}^{(n)}(s) \equiv U_{\mu}^{(n)\dagger}(s - \hat{\mu})$ . Here,  $\alpha \in \mathbb{R}$  is referred to as the smearing parameter, which controls the speed of the smearing. The summation index  $j$  runs over only the spatial directions to avoid the artificial nonlocality in time. A schematic illustration of  $V_i^{(n)}(s)$  is shown in Fig. 1.  $U_i^{(n+1)}(s)$  is the closest SU(3) element to  $V_i^{(n)}(s)$ . It is easy to see that  $V_i^{(n)}(s)$  and  $U_i^{(n+1)}(s)$  hold the same gauge transformation properties with  $U_i^{(n)}(s)$ . Hence, the smearing method respects the gauge covariance. As the physically extended glueball operator, we adopt the  $n$ -th smeared operator, i.e., the plaquette operator which is constructed with the  $n$ -th fat link variables  $U_i^{(n)}(s)$ .

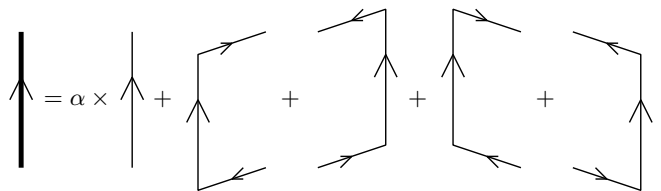


FIG. 1: The schematic illustration of  $V_i^{(n)}(s)$ . The thick line represents the variable  $V_i^{(n)}(s)$ . Thin lines represent the link variables  $U_i^{(n)}(s)$ .

## C. The physical meaning of the smearing method

Here, we estimate the size of the  $n$ -th smeared operator and consider the physical meaning of the smearing

method. To obtain the direct correspondence with the continuum theory, we adopt the lattice Coulomb gauge, which is defined so as to maximize

$$R \equiv \sum_s \sum_{k=1}^3 \text{ReTr} U_k(s), \quad (14)$$

with respect to SU(3) gauge transformations. In the continuum limit, we recover the continuum Coulomb gauge condition as

$$\sum_{k=1}^3 \partial_k A_k(x) = 0. \quad (15)$$

In this gauge, the spatial link-variable  $U_k(s)$  becomes maximally continuous around 1, and can be safely expanded in  $a$  as  $U_k(s) \equiv e^{iaA_k(s)} = 1 + iaA_k(s) + O(a^2)$  near the continuum limit. We consider the smearing with the smearing parameter  $\alpha$ . For convenience, we define

$$p \equiv \frac{\alpha}{\alpha + 4}, \quad q \equiv \frac{1}{\alpha + 4}, \quad (16)$$

which satisfy  $p + 4q = 1$ . As shown in Fig. 1, the  $(n+1)$ -th smeared spatial gluon field  $A_k(s; n+1)$  is iteratively described with the  $n$ -th smeared gluon field  $A_k(s; n)$  as

$$\begin{aligned} A_x(s; n+1) &= pA_x(s; n) + q \left( A_y(s; n) + A_x(s + \hat{y}; n) - A_y(s + \hat{x}; n) - A_y(s - \hat{y}; n) + A_x(s - \hat{y}; n) + A_y(s + \hat{x} - \hat{y}; n) \right. \\ &\quad \left. + A_z(s; n) + A_x(s + \hat{z}; n) - A_z(s + \hat{x}; n) - A_z(s - \hat{z}; n) + A_x(s - \hat{z}; n) + A_z(s + \hat{x} - \hat{z}; n) \right) \end{aligned} \quad (17)$$

in the leading order in  $a$ . The expressions for  $A_y(s; n+1)$  and  $A_z(s; n+1)$  are similar. After some rearrangements, we obtain in the leading order in  $a$

$$\begin{aligned} \partial_n A_x(s; n) &\equiv A_x(s; n+1) - A_x(s; n) \\ &= q \left\{ \partial_y A_x(s; n) - \partial_y A_x(s - \hat{y}; n) \right. \\ &\quad \left. + \partial_z A_x(s; n) - \partial_z A_x(s - \hat{z}; n) \right. \\ &\quad \left. - \partial_x A_y(s; n) + \partial_x A_y(s - \hat{y}; n) \right. \\ &\quad \left. - \partial_x A_z(s; n) + \partial_x A_z(s - \hat{z}; n) \right\} \\ &= q \left\{ (\partial_x^B \partial_x + \partial_y^B \partial_y + \partial_z^B \partial_z) A_x(s; n) \right. \\ &\quad \left. - \partial_x \sum_{k=1}^3 \partial_k^B A_k(s; n) \right\}. \end{aligned} \quad (18)$$

Here,  $\partial_k$  and  $\partial_k^B$  denote the forward and backward difference operators along  $k$ -axis ( $k = x, y, z$ ), respectively, which are defined as

$$\partial_k f(s) \equiv f(s + \hat{k}) - f(s), \quad \partial_k^B f(x) \equiv f(s) - f(s - \hat{k}), \quad (19)$$

respectively. Here,  $\hat{k}$  denotes the unit vector along the  $k$ -axis. By applying the continuum approximation both with respect to  $s$  and  $n$ , the difference operators  $\partial_n$ ,  $\partial_k$  and  $\partial_k^B$  are then replaced by the derivatives  $a_n \partial / \partial \tilde{n}$ ,  $a_s \partial / \partial x_k$  and  $a_s \partial / \partial x_k$ , respectively. Here,  $\tilde{n} \equiv n a_n$  is the continuum parameter corresponding to  $n$ , and  $a_n \in \mathbb{R}$  is formally introduced as a small constant interval in the  $n$ -direction, although the final result does not depend on  $a_n$  at all. In the continuum Coulomb gauge using Eq. (15),

Eq. (18) reduces to the diffusion equation

$$a_n \frac{\partial}{\partial \tilde{n}} A_i(\vec{x}; n) = D \Delta A_i(\vec{x}; n) \quad \text{for } i = x, y, z, \quad (20)$$

where  $D \equiv \frac{a_s^2}{\alpha + 4}$  works as the diffusion parameter. By solving this equation, the  $n$ -th smeared gauge field  $A_i(\vec{x}; n)$  can be expressed by a linear combination of the original gluon field  $A_i(\vec{x})$  as

$$\begin{aligned} A_i(\vec{x}; n) &= \int d^3 y K(\vec{x} - \vec{y}; n) A_i(\vec{y}) \\ K(\vec{x}; n) &\equiv \frac{1}{\pi^{3/2} \rho^3} \exp\left(-\frac{\vec{x}^2}{\rho^2}\right), \end{aligned} \quad (21)$$

where the Gaussian extension  $\rho$  is defined as

$$\rho \equiv 2\sqrt{Dn} = 2a_s \sqrt{\frac{n}{\alpha + 4}}. \quad (22)$$

In this way, the  $n$ -th smeared gluon field physically corresponds to the Gaussian-distributed operator of the original gluon field. After the linearization of the gluon field, the  $n$ -th smeared plaquette is also expressed as the Gaussian-distributed operator. Here, the Gaussian extension  $\rho$  can be regarded as a characteristic size of the  $n$ -th smeared operator.

The expression of  $\rho$  in Eq. (22) explains the physical roles of the two parameters,  $\alpha$  and  $n$ . The smearing parameter  $\alpha$  plays the role of controlling the speed of the smearing, while, for each fixed  $\alpha$ ,  $n$  plays the role of extending the size of the smeared operator. Note that, for the larger  $\alpha$ , the speed of smearing is the slower.

The smearing method was originally introduced to carry out the accurate mass measurement by maximizing

the ground-state overlap [28]. However, we will use it to give a rough estimate of the physical glueball size. In fact, once we find the pair of the smearing parameters  $n$  and  $\alpha$ , which achieves the maximum ground-state overlap, the physical size of the glueball is roughly estimated with Eq. (22).

With Eq. (21), we try to express the  $n$ -th smeared  $0^{++}$  glueball operator in terms of the original gluon field  $A_\mu^a(x)$ . Near the continuum limit, the zero-momentum projected  $0^{++}$  glueball operator  $\Phi_{\text{GB}}(0^{++}; n)$  consisting

of the smeared link-variable  $U_i^{(n)}(s)$  is expressed as

$$\Phi_{\text{GB}}(0^{++}; n) = \frac{1}{V} \int d^3x G_{ij}^a(\vec{x}, t; n) G_{ij}^a(\vec{x}, t; n), \quad (23)$$

where  $G_{ij}^a(\vec{x}, t; n)$  is the field strength associated with the smeared gluon field  $A_i^a(\vec{x}, t; n)$ . Here,  $t$  can be regarded as a fixed parameter in this argument, and will be omitted hereafter. By inserting Eq. (21),  $\Phi_{\text{GB}}(0^{++})$  is expressed with the original gauge field  $A_i^a(\vec{x})$  as

$$\begin{aligned} \Phi_{\text{GB}}(0^{++}; n) &= \frac{1}{V} \int d^3x \int d^3y d^3z \left( \frac{\partial}{\partial x_i} K(\vec{x} - \vec{y}; n) A_j(\vec{y}) - \frac{\partial}{\partial x_j} K(\vec{x} - \vec{y}; n) A_i(\vec{y}) \right) \\ &\quad \times \left( \frac{\partial}{\partial x_i} K(\vec{x} - \vec{z}; n) A_j(\vec{z}) - \frac{\partial}{\partial x_j} K(\vec{x} - \vec{z}; n) A_i(\vec{z}) \right) + \dots \\ &= \frac{2}{V} \int \frac{d^3y d^3z}{\pi^{3/2} \rho^3} \exp\left(-\frac{(\vec{y} - \vec{z})^2}{2\rho^2}\right) \frac{\partial}{\partial y_j} A_i(\vec{y}) \frac{\partial}{\partial z_j} A_i(\vec{z}) + \dots \\ &= \frac{2}{V} \int \frac{d^3y d^3z}{\pi^{3/2} \rho^5} \left( 3 - \frac{(\vec{y} - \vec{z})^2}{\rho^2} \right) \exp\left(-\frac{(\vec{y} - \vec{z})^2}{2\rho^2}\right) A_i(\vec{y}) A_i(\vec{z}) + \dots \end{aligned} \quad (24)$$

Here, “...” represents the terms which are more than quadratic in the gluon field, and are dropped off. In this derivation, partial integrations and the Coulomb gauge condition have been used. We expect that  $\Phi_{\text{GB}}(0^{++}, n)$  is associated with the best pair of the smearing parameters  $n$  and  $\alpha$  and works as an approximate “creation” operator of the  $0^{++}$  glueball, which creates an approximate single glueball state from the vacuum.

#### D. The relation to Bethe-Salpeter amplitude

In the previous subsection, we proposed one possible method to give a rough estimate of the glueball size. In this subsection, we consider the relation between our estimate of the glueball size and the other estimate from the Bethe-Salpeter (BS) amplitude, which was adopted in Refs.[31].

The size of the glueball is actually a nontrivial quantity. Although the charge radius of the glueball can be formally defined, its electric charges are carried by the

quarks and anti-quarks, which play only of secondary roles in describing the glueball state in the idealized limit, since the glueball by its nature does not contain any valence contents of (anti-)quarks.

In order to investigate the size of the glueball, the BS amplitude provides a convenient tool. The BS amplitude  $\Psi(\vec{x}, \vec{y})$  is expressed as

$$\Psi_{\text{BS}}(\vec{y}, \vec{z}) \equiv \langle 0 | A_i(\vec{y}) A_i(\vec{z}) | G(\vec{P} = \vec{0}) \rangle, \quad (25)$$

which can be obtained as a solution of the BS equation. In the non-relativistic limit, it is expected to reduce to the glueball wave function in the first-quantized picture. This property has been exploited to estimate the size of the glueball in Ref.[31].

The connection between these two estimates is provided with Eq. (24) in the following way. We consider  $\Phi_{\text{GB}}(0^{++}; n)$  associated with the best smearing with the Gaussian extension  $\rho$ . Since the ground-state overlap is maximized, the  $0^{++}$ -glueball state can be approximated as

$$\begin{aligned} |G(\vec{P} = \vec{0})\rangle &\simeq \Phi_{\text{GB}}(0^{++}; n) |0\rangle \\ &= \frac{2}{V} \int \frac{d^3y d^3z}{\pi^{3/2} \rho^5} \left( 3 - \frac{(\vec{y} - \vec{z})^2}{\rho^2} \right) \exp\left(-\frac{(\vec{y} - \vec{z})^2}{2\rho^2}\right) |A_i(\vec{y}) A_i(\vec{z})\rangle + \dots \\ &= \frac{2}{\pi^{3/2} \rho^5} \int d^3r \left( 3 - \frac{\vec{r}^2}{\rho^2} \right) \exp\left(-\frac{\vec{r}^2}{2\rho^2}\right) |A_i(\vec{r}) A_i(\vec{0})\rangle + \dots, \end{aligned} \quad (26)$$

where we exploit the translational invariance and partial

integrations. Similar to Eq. (24), the states in Eq. (26)

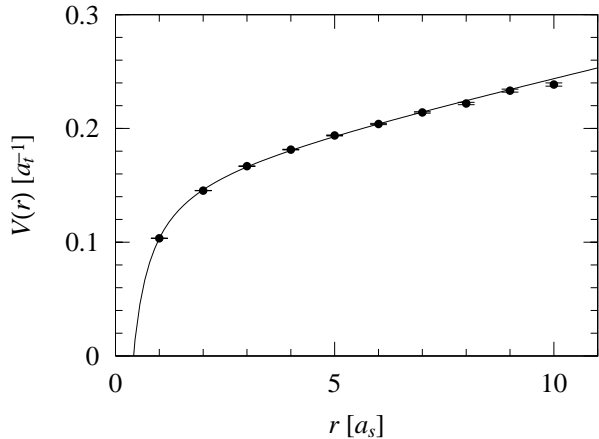


FIG. 2: The inter-quark potential plotted against the inter-quark separation  $r$ . The solid circles denote the on-axis data of the inter-quark potential. The solid line represents the result of the best-fit analysis with Eq. (30).

such as  $|G(\vec{P} = \vec{0})\rangle$  and  $|A_i(\vec{y})A_i(\vec{z})\rangle$  are obtained with the gauge configuration generated in lattice QCD. Hence, this relation would provide a kind of nonperturbative construction of the glueball state in terms of the gluon field.

In the constituent gluon picture [32], the BS amplitude associated with Eq. (26) reduces to the following expression as

$$\Psi_{\text{BS}}(\vec{r}, \vec{0}) \simeq \frac{2}{\pi^{3/2}\rho^5} \left(3 - \frac{\vec{r}^2}{\rho^2}\right) \exp\left(-\frac{\vec{r}^2}{2\rho^2}\right), \quad (27)$$

in the heavy effective gluon mass limit.

### III. ANISOTROPIC LATTICE QCD

#### A. Lattice Parameter Set

We use the SU(3) plaquette action on an anisotropic lattice

$$S_G = \frac{\beta_{\text{lat}}}{N_c} \frac{1}{\gamma_G} \sum_{s,i < j \leq 3} \text{ReTr} \left(1 - P_{ij}(s)\right) + \frac{\beta_{\text{lat}}}{N_c} \gamma_G \sum_{s,i \leq 3} \text{ReTr} \left(1 - P_{i4}(s)\right), \quad (28)$$

where  $P_{\mu\nu}(s) \in \text{SU}(3)$  denotes the plaquette operator in the  $\mu$ - $\nu$ -plane. The lattice parameter and the bare anisotropy parameter are fixed as  $\beta_{\text{lat}} \equiv 2N_c/g^2 = 6.25$  and  $\gamma_G = 3.2552$ , respectively, so as to reproduce the renormalized anisotropy  $\xi \equiv a_s/a_t = 4$  [20]. We adopt the pseudo-heat-bath algorithm for the update of the gauge field configurations in the Monte Carlo calculation.

To measure the glueball correlators, we perform the numerical calculations on the lattice of the sizes  $20^3 \times N_t$  with various  $N_t$  as  $N_t =$

24, 26, 28, 30, 33, 34, 35, 36, 37, 38, 40, 43, 45, 50, 72, which correspond to the various temperatures listed in Table I. For all temperatures, we pick up gauge field configurations every 100 sweeps for measurements, after skipping more than 20,000 sweeps for the thermalization. The numbers  $N_{\text{conf}}$  of gauge configurations used in our calculations are summarized in Table I.

We divide the data into bins of the size 100 to reduce the possibly strong auto-correlations. However, the auto-correlations are not observed so strong in this simulation with the 100 sweep separation, since the separation by 100 sweeps seems already rather large. *Unless otherwise stated, the statistical errors are understood to be estimated with the jackknife analysis by regarding each bin as an independent data point throughout in this paper.*

As for the smearing parameters, which play the important role in extracting the ground-state contribution, we have checked that one of the best sets is provided as

$$\alpha = 2.1, \quad N_{\text{smr}} = 40, \quad (29)$$

in the present lattice calculation for the lowest  $0^{++}$  and  $2^{++}$  glueballs. As we shall see later, the temporal correlator  $G(t)/G(0)$  and the pole mass  $m_G$  are almost insensitive to a particular choice of the smearing number  $N_{\text{smr}}$ , as far as  $N_{\text{smr}} \sim 40$  with  $\alpha = 2.1$ . In fact, in the rather wide range as  $30 \lesssim N_{\text{smr}} \lesssim 50$ ,  $G(t)/G(0)$  and  $m_G$  are almost unchanged, and the ground-state overlap  $C$  is kept almost maximized. (See Fig. 7.) *Unless otherwise stated, we adopt the smearing with Eq. (29) in this paper.* Only for the accurate measurement, we seek for the best value of  $N_{\text{smr}}$  with  $\alpha = 2.1$  fixed, although the results are almost the same as those with  $N_{\text{smr}} = 40$ .

In this paper, we only consider the case with  $\alpha = 2.1$ . The essential point of the smearing method is to construct an operator which has the same size with the physical glueball size in order to improve the ground-state overlap [28]. Hence, a different pair of the smearing parameters  $(\alpha', N'_{\text{smr}})$  would work as good as the original  $(\alpha, N_{\text{smr}})$  does, provided that these two pairs of the smearing parameters correspond to the same operator size. However, we have to take into account the following points when picking up the value of  $\alpha$ . On the one hand, the speed of the smearing is the faster for the smaller  $\alpha$ , which, however, results in the coarser discretization in  $n$  in Eq. (20). Hence,  $\alpha$  has to be enough large so as to construct the ground-state glueball operator. We have checked that  $\alpha > 2.0$  seems to work well. On the other hand, if we adopt the larger value of  $\alpha$ , the speed of the smearing becomes the slower. Hence, we have to scan the wider range of  $N_{\text{smr}}$  to maximize the overlap. A practical solution is provided by  $\alpha = 2.1$ , since it is one of the smallest possible values of  $\alpha$ , which, in the same time, corresponds to enough fine discretization in  $n$  in Eq. (20).

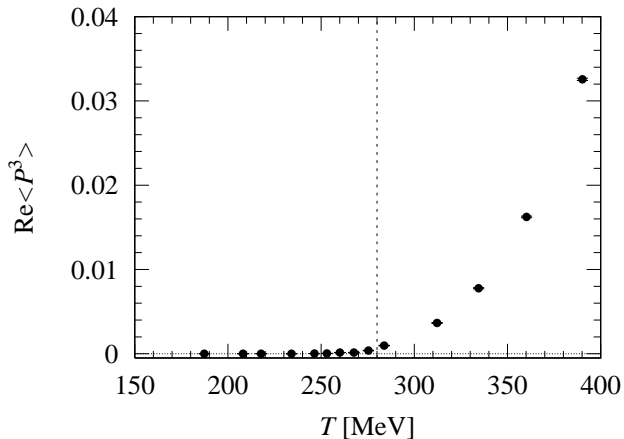


FIG. 3: The cubed Polyakov loop  $\text{Re}\langle P^3 \rangle$  plotted against temperature. The vertical dotted line denotes the estimated critical temperature,  $T_c \simeq 280$  MeV. The error bars are hidden inside the symbols.

### B. Determination of lattice spacings

In order to evaluate the spatial and temporal lattice spacings,  $a_s$  and  $a_t$ , we perform a separate Monte Carlo simulation on the lattice of the size  $20^3 \times 80$ . Here, we skip 10,000 sweeps for the thermalization, and pick up gauge configurations every 500 sweeps for measurement of the static inter-quark potential. The statistical data are divided into bins of the size 2, where each bin is thought of as an independent data point. In Fig. 2, the inter-quark potential is shown. We adopt the parameterization of the inter-quark potential as

$$V(r) = C - \frac{A}{r} + \sigma r, \quad (30)$$

where  $C$ ,  $A$ ,  $\sigma$  denote the offset, the Coulomb coefficient, and the string tension, respectively. By fitting the on-axis data with  $V(r)$ , we obtain  $C = 0.16217(53)$ ,  $A = 0.06758(42)$  and  $\sigma = 0.00883(12)$ . Hence, by assuming  $\sqrt{\sigma} = 440$  MeV, the lattice spacings are obtained as

$$a_s^{-1} = 2.341(16)\text{GeV}, \quad a_t^{-1} = 9.365(66)\text{GeV}, \quad (31)$$

namely,  $a_s \simeq 0.084$  fm and  $a_t \simeq 0.021$  fm. Hence, the spatial lattice size of 20 corresponds to 1.68 fm in the physical unit.

### C. The critical temperature

Here, for completeness, we give an estimate of the critical temperature  $T_c$  on our anisotropic lattice, although the value of  $T_c \simeq 260$  MeV with  $\sqrt{\sigma} \simeq 420$  MeV is rather established on the isotropic lattice [4].

To estimate the critical temperature  $T_c$ , we consider

the Polyakov loop, which is defined as

$$\begin{aligned} P &\equiv \frac{1}{V} \int d^3x \text{Tr} \left( T \exp i \int_0^\beta dt A_0(\vec{x}, t) \right) \\ &= \frac{1}{V} \int d^3x \text{Tr} \left( U_4(\vec{x}, 0) \cdots U_4(\vec{x}, N_t - 1) \right), \end{aligned} \quad (32)$$

where  $V$  denotes the volume of the space and  $T$  the time-ordering operation. As is well-known, its thermal expectation value  $\langle P \rangle = \frac{1}{N_{\text{conf}}} \sum_{k=1}^{N_{\text{conf}}} P_k$ , averaged over lots of gauge configurations, is an order parameter of quark confinement associated with the center  $\mathbb{Z}_3$  symmetry [25, 26], where  $P_k$  denotes the value of the Polyakov loop  $P$  with the  $k$ -th configuration. However, to be strict, it is only in the thermodynamic limit with the infinite volume that Eq. (32) can work as the order parameter to estimate  $T_c$ . Note that, since the size of the lattice is limited, tunnelings from one vacuum to another are unavoidable for large simulation time even in the  $\mathbb{Z}_3$  broken phase. As a consequence, due to the associated cancellation of the center  $\mathbb{Z}_3$ -phase factor,  $\langle P \rangle$  finally vanishes on the finite lattice, which raises a technical difficulty in estimating  $T_c$  from  $\langle P \rangle$ . To avoid this, instead of using the total expectation value itself, one often analyzes the scattering plot, a plot of  $P_k$  for each configuration labeled by  $k$ .

Here, for convenience, we analyze the thermal expectation value of the cubed Polyakov loop as

$$\langle P^3 \rangle = \frac{1}{N_{\text{conf}}} \sum_{k=1}^{N_{\text{conf}}} (P_k)^3, \quad (33)$$

which provides the equivalent result for the estimate of the critical temperature  $T_c$  with the scattering plot. We note that  $\langle P^3 \rangle$  is not the order parameter of the confinement phase in a strict sense, since it is invariant under the center  $\mathbb{Z}_3$  transformation. In general, in the symmetric phase, the expectation value of the order parameter vanishes due to the cancellation of the phase factor associated with the symmetry transformations, which never happens in the broken symmetry phase. However, in the specific case of  $\langle P \rangle$ , it is known from the analysis of the scattering plot that the norm of  $P_k$  for each configuration is already quite small in the symmetric phase, due to which its expectation value  $\langle P \rangle$  almost vanishes even without involving the cancellation of the center  $\mathbb{Z}_3$  phase factor. In contrast,  $P_k$  takes a manifestly non-vanishing value for each configuration in the broken symmetry phase, which can be used to identify the critical temperature  $T_c$ .

Such a tendency is quantitatively described with the cubed Polyakov loop  $\langle P^3 \rangle$ . In fact, in the plot of  $\langle P^3 \rangle$  versus temperature  $T$ , the critical temperature  $T_c$  is characterized as the point where it begins to have a non-vanishing value.

In Fig. 3,  $\langle P^3 \rangle$  is plotted against temperature. By taking into account the finite size effects which smoothen the



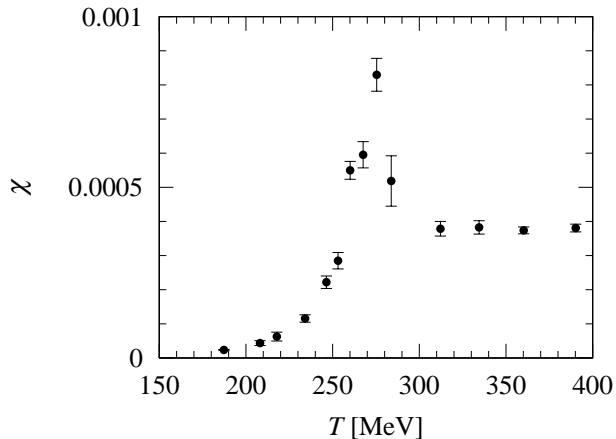


FIG. 4: The susceptibility  $\chi$  of the Polyakov-loop plotted against the temperature. There is a sharp peak around  $T = 280$  MeV, which indicates the critical temperature  $T_c$  of the phase transition in quenched SU(3) QCD.

phase transition, we estimate the critical temperature as  $T_c \simeq 260\text{--}280$  MeV, which is consistent with the previous studies in Ref. [4], i.e.,  $T_c/\sqrt{\sigma} = 0.629(3)$ .

For more accurate determination of the critical temperature  $T_c$ , we investigate the Polyakov-loop susceptibility  $\chi$ , which is defined as [30]

$$\chi \equiv \langle \Omega^2 \rangle - \langle \Omega \rangle^2 \quad (34)$$

$$\Omega \equiv \begin{cases} \text{Re}P \exp(-2\pi i/3), & \arg P \in [\pi/3, \pi), \\ \text{Re}P, & \arg P \in [-\pi/3, \pi/3), \\ \text{Re}P \exp(2\pi i/3), & \arg P \in [-\pi, -\pi/3). \end{cases}$$

In Fig. 4, the Polyakov loop susceptibility is plotted against temperature. To obtain  $\chi$ , about 3,000 gauge configurations are used at each temperature near  $T_c$ , which are divided into bins of the size 50. The statistical errors are estimated with the jackknife analysis. We observe that a sharp peak is located between  $T = 275$  MeV and  $T = 284$  MeV. Hence, we identify the critical temperature of our lattice as  $T_c \simeq 280$  MeV.

#### IV. NUMERICAL RESULTS —TEMPORAL CORRELATIONS AND POLE-MASSSES

In this section, we construct the temporal glueball correlator  $G(t)$  at finite temperature, and perform the pole-mass measurement. We adopt the procedure used in [13] as the standard one to extract the pole-mass  $m_G(T)$  of the thermal glueball from the temporal correlator  $G(t)$  at temperature  $T$  by using the best-fit analysis with the fit function of single-cosh type considered later. Here, we regard each glueball as a quasi-particle and assume that the thermal width  $\Gamma$  of the ground-state peak is enough narrow in the spectral function  $\rho(\omega)$ . From the viewpoint

of the spectral representation Eq. (5), such a narrowness of the peak is necessary to identify the pole-mass as a definite object and also to justify this standard procedure in a strict sense. (In Sect. V, we will analyze our lattice QCD data without assuming the narrowness of the peak as a straightforward extension to the current analysis.)

Suppose that the thermal width is sufficiently narrow, i.e.,  $\Gamma \simeq 0$ . Then, the spectral function  $\rho(\omega)$  receives the contribution from the ground-state in the following manner:

$$\rho(\omega) = 2\pi A \left( \delta(\omega - m_G) - \delta(\omega + m_G) \right) + \dots, \quad (35)$$

where “...” represents the contributions from excited-states, and  $A \equiv A(T)$  and  $m_G \equiv m_G(T)$  are the strength and the pole-mass of the glueball peak at temperature  $T$ , respectively. Note that the appearance of the second delta function is due to the fact that the spectral function  $\rho(\omega)$  is odd in  $\omega$ , which reflects the bosonic nature of the glueball. Corresponding to Eq. (35), by inserting it into the spectral representation Eq. (5), the ground state contribution to the temporal correlator  $G(t)$  is expressed as

$$G(t) = \frac{A}{1 - e^{-\beta m_G}} \left( e^{-tm_G} + e^{-(\beta-t)m_G} \right) + \dots. \quad (36)$$

Hence, after the ground state contribution is sufficiently enhanced, the appropriate fit function for  $G(t)/G(0)$  is the following single hyperbolic cosine as

$$g(t) \equiv C \left( e^{-tm_G} + e^{-(\beta-t)m_G} \right), \quad (37)$$

where  $C$  and  $m_G$  are understood as the fit parameters. We will refer to  $C$  as the ground-state overlap, and to the fit function of  $g(t)$  as the fit function of single-cosh type for simplicity.

For the accurate measurement, it is required that  $G(t)$  is dominated by the ground-state contribution in the fit-range. (We consider the determination of the fit range in the next subsection with an explicit example.) In this case,  $g(t)$  can properly represent the ground-state contribution in Eq. (36), and  $C$  and  $m_G$  can be extracted accurately. In the actual calculations, the complete elimination of all the remaining contributions of the excited states is impossible. Since each hyperbolic cosine component contributes to  $G(t)$  positively as is seen in the spectral representation Eq. (5), we always have the following inequalities as

$$g(0) \leq 1, \text{ and } C = \frac{g(0)}{1 + e^{-\beta m_G}} \leq \frac{1}{1 + e^{-\beta m_G}}. \quad (38)$$

Here,  $g(0)$  and  $C$  take their maxima, if and only if  $G(t)$  is completely dominated by the ground-state contribution in the whole region  $0 \leq t \leq \beta$ . In this case, we have the following equalities instead:

$$g(0) = 1, \text{ and } C = \frac{1}{1 + e^{-\beta m_G}}. \quad (39)$$

We thus see that  $g(0) \simeq 1$  and  $C \simeq 1/(1 + e^{-\beta m_G}) \simeq 1$  can both work as a criterion to determine whether the ground-state enhancement is sufficient or not. We will refer to  $g(0)$  as the normalized ground-state overlap. Note that  $C$  differs from  $g(0)$  only through the factor  $1/(1 + e^{-\beta m_G})$ , which is independent of both the smearing parameters  $\alpha$  and  $N_{\text{smr}}$ . In this section, we examine  $C$  to determine if the ground-state enhancement is sufficient or not. We prefer  $C$  rather than  $g(0)$  because of the following reasons. (i) The ground-state overlap  $C$  is directly obtained from the best-fit analysis with Eq. (37) as one of the best-fit parameters. (ii) In our previous work [16],  $C$  has been used for the criterion. However,  $g(0) \simeq 1$  has the advantage over  $C \simeq 1$  in Sect. V, where the counterpart of  $C$  cannot be properly defined, whereas the counterpart of  $g(0)$  can. At any rate, as is seen in Tables I and II, they are not so different from each other in numerical value, especially below  $T_c$ .

### A. Thermal $0^{++}$ glueball

In Fig. 5 (a), we show the  $0^{++}$  glueball correlator for the low temperature case  $T = 130$  MeV after the suitable smearing as Eq. (29). We perform the best-fit analysis of the single-cosh type Eq. (37) with the two fit parameters, the ground-state overlap  $C$  and the pole-mass  $m_G$  of the lowest thermal glueball. The solid line denotes the result of this best-fit analysis. The fit-range is indicated by the vertical dotted lines.

#### 1. The fit range

We consider the determination of the fit-range. Even after the ground-state enhancement is performed, the complete elimination of all the contributions of the excited states is impossible, especially in the neighborhood of  $t \sim 0 \pmod{\beta}$ . It follows that the equality Eq. (36) holds only in a limited interval, which does not include the neighborhood of  $t \sim 0$ . Hence, for the accurate measurement of the pole-mass  $m_G$ , we need to find the appropriate fit-range, where contributions from excited states almost die out. To this end, we examine the effective-mass plot. The effective mass  $m_{\text{eff}}(t)$  is defined as the solution to the following equation as

$$G(t+1)/G(t) = \frac{\cosh\left((t+1 - N_t/2)a_t m_{\text{eff}}(t)\right)}{\cosh\left((t - N_t/2)a_t m_{\text{eff}}(t)\right)}, \quad (40)$$

for a given  $G(t+1)/G(t)$  at each fixed  $t$ . In Fig. 5 (b), we plot the effective mass  $m_{\text{eff}}(t)$  against  $t$  associated with Fig. 5 (a). We see that there appears a plateau, a region where  $m_{\text{eff}}(t)$  takes almost a constant value. In this region, it is expected that  $G(t)$  consists of nearly a single spectral component, and, hence,  $g(t)$  can properly represent the ground-state contribution in Eq. (36). Note

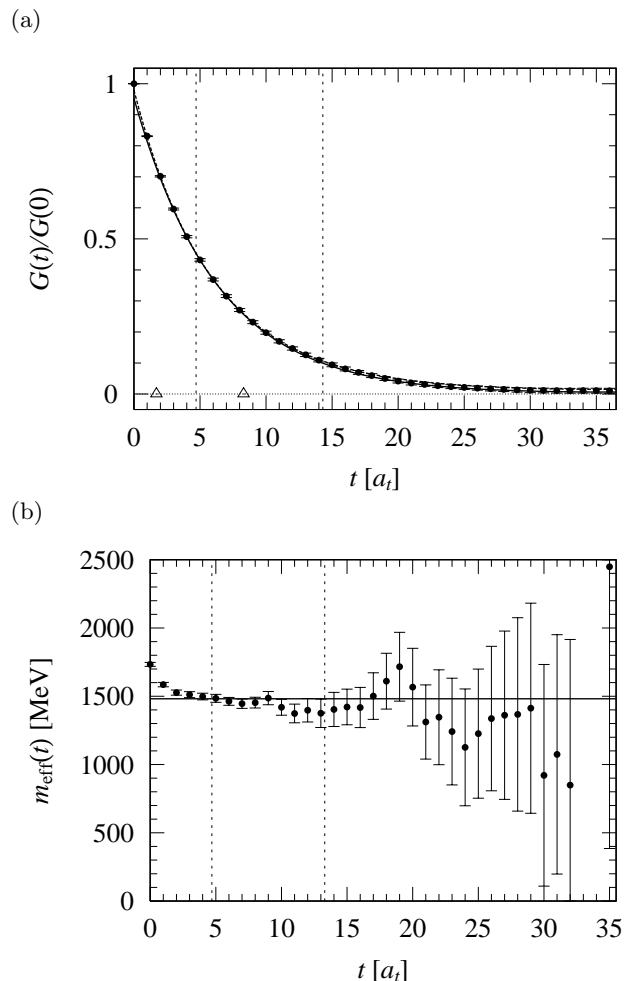


FIG. 5: (a) The temporal correlator  $G(t)/G(0)$  of the  $0^{++}$  glueball at the low temperature ( $T = 130$  MeV). (b) The corresponding cosh-type effective-mass plot. In both figures, the solid lines represent the best single hyperbolic-cosine fitting in the plateau, which is indicated by the vertical dotted lines. The dashed curve in (a) denotes the result of the best-fit analysis of Breit-Wigner type performed in the interval indicated by the two open triangles. (See Sect. V and Eq. (50) for detail.)

that, if more than a single state contribute with their different masses, a nontrivial  $t$ -dependence will appear in  $m_{\text{eff}}(t)$ . In the zero-temperature case, the plateau in the effective-mass plot is widely used as a candidate for the fit range in the best-fit analysis of single-cosh type Eq. (37). Here, the role of the smearing method is to suppress the excited-state contributions as much as possible, so that the plateau can be obtained with the smallest possible  $t$ .

In Fig. 5 (b), the plateau is indicated by the vertical dotted lines, which is used to determine the fit-range. In this low temperature case  $T = 130$  MeV, the best-fit analysis shows  $C = 0.953(7)$  and  $m_G = 1482(25)$  MeV, which seems consistent with  $m_G \simeq 1500\text{--}1700$  MeV at  $T \simeq 0$  MeV. We note that the ground-state overlap  $C = 0.95$  becomes enough large owing to the suitable

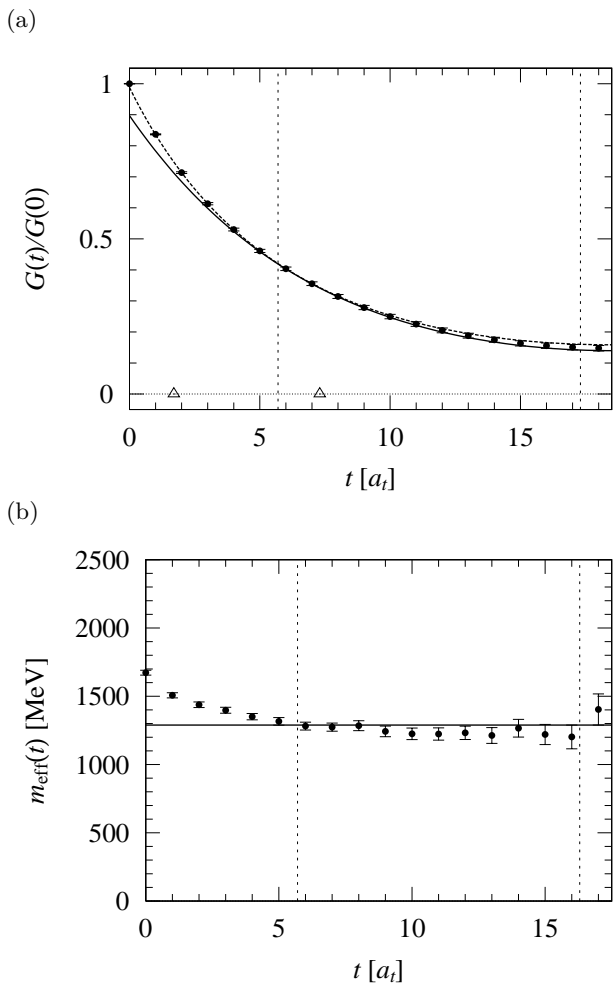


FIG. 6: (a) The temporal correlator  $G(t)/G(0)$  of the  $0^{++}$  glueball at the high temperature ( $T = 253$  MeV). (b) The corresponding cosh-type effective-mass plot. The meaning of the solid lines in both figures and the dashed curve in (a) are the same as in Fig. 5.

smearing.

In Fig. 6 (a), we show the  $0^{++}$  glueball correlator for the high temperature case  $T = 253$  MeV ( $< T_c$ ) after the suitable smearing as Eq. (29). The solid line denotes the result of the best-fit analysis of the single-cosh type. The fit-range is indicated by the vertical dotted lines, which is determined from the plateau in the corresponding effective-mass plot Fig. 6 (b). We obtain  $C = 0.89(1)$  and  $m_G = 1289(26)$  MeV. Owing to the suitable smearing, contributions from the excited state are seen suppressed ( $C \simeq 1$ ).

## 2. The ground-state overlap

In Fig. 7, the ground-state overlap  $C$  and the pole-mass  $m_G$  for the  $0^{++}$  glueball are plotted against the smearing number  $N_{\text{smr}}$  for the two cases (i) the low temperature case  $T = 130$  MeV (circle), (ii) the high temperature case

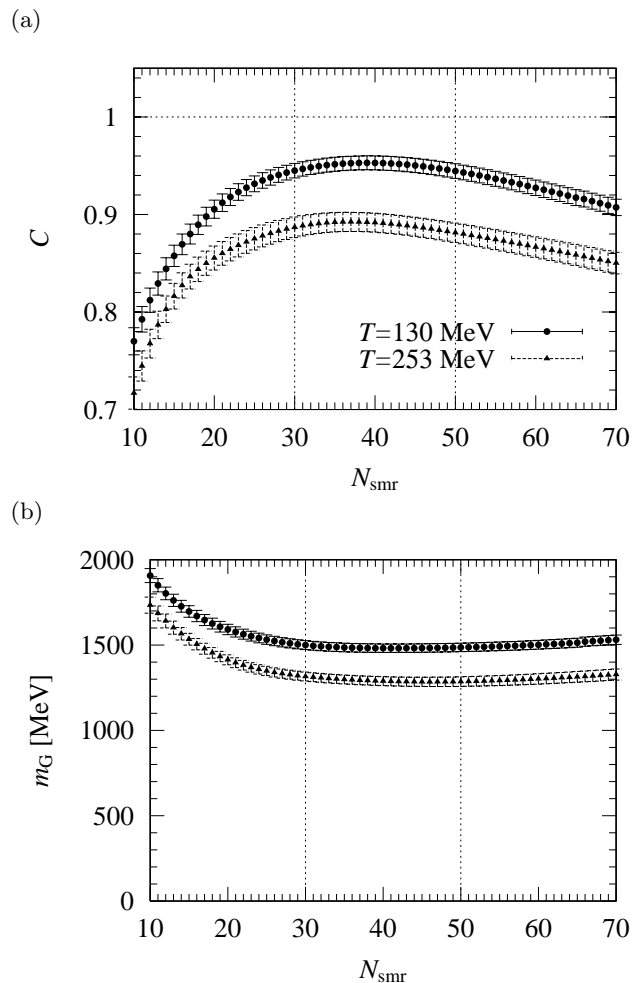


FIG. 7: (a) The ground-state overlap  $C$  and (b) the glueball mass  $m_G$  plotted against the smearing number  $N_{\text{smr}}$  for the temperatures  $T = 130, 253$  MeV. The solid circle corresponds to  $T = 130$  MeV, and the solid triangle to  $T = 253$  MeV. The suitable smearing is found to be in a range as  $30 < N_{\text{smr}} < 50$ , where  $C$  is kept maximized and  $m_G$  is kept minimized simultaneously.

$T = 253$  MeV (triangle) below  $T_c$ . Here, we fix one of the smearing parameters as  $\alpha = 2.1$ . We see that, in the region  $N_{\text{smr}} < 30$ , with increasing  $N_{\text{smr}}$ , the ground state overlap  $C$  is growing and the pole-mass  $m_G$  is reducing. Then, in the region  $30 < N_{\text{smr}} < 50$ ,  $C$  is kept maximized and  $m_G$  is kept minimized, which implies that the ground-state contribution in  $G(t)$  is maximally enhanced. Beyond this region, i.e., for  $N_{\text{smr}} > 50$ , since the size of the smeared operator exceeds the physical size of the glueball,  $C$  begins to decline and  $m_G$  begins to grow gradually.

The maximum overlap and the minimum mass should be achieved at almost the same  $N_{\text{smear}}$ . In fact, both of these two conditions should work as an indication of the maximally enhanced ground-state contribution. In practical calculations, these two conditions are achieved at slightly different  $N_{\text{smear}}$ . However, the numerical results

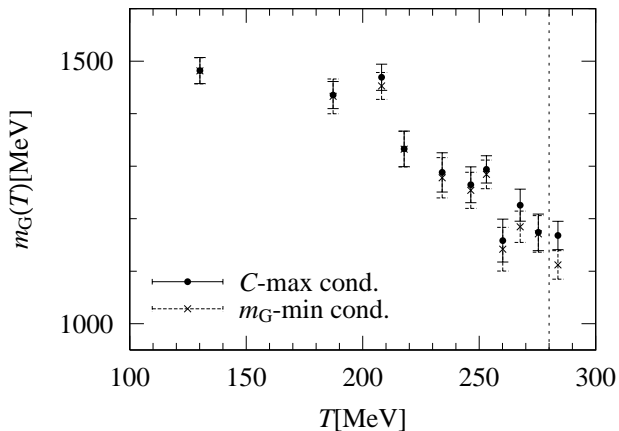


FIG. 8: The  $0^{++}$  glueball mass  $m_G(T)$  plotted against temperature  $T$ . The solid circle and the cross denote the thermal  $0^{++}$  glueball mass obtained with the maximum overlap condition and the mass minimum condition, respectively. The vertical dotted line indicates the critical temperature  $T_c \simeq 280$  MeV in quenched QCD.

on the pole-mass are almost the same. For instance, from Fig. 7, the former condition leads to  $m_G(T = 130\text{MeV}) = 1482(25)$  MeV at  $N_{\text{smear}} = 39$  and  $m_G(T = 253\text{MeV}) = 1294(26)$  MeV at  $N_{\text{smear}} = 37$ , while the latter condition leads to  $m_G(T = 130\text{MeV}) = 1481(25)$  MeV at  $N_{\text{smear}} = 41$  and  $m_G(T = 253\text{MeV}) = 1284(27)$  MeV at  $N_{\text{smear}} = 46$ .

As we mentioned before, we divide the statistical data into the bins of the size 100 to reduce the possible auto-correlations. However, the bin-size dependence is not seen so strong even in the vicinity of the critical temperature  $T_c$ . Recall that the measurement interval of the gauge field configuration is 100 sweeps. Since this interval is already rather large, the bin-size of 100 seems to be sufficient to overcome the auto-correlations. This is also the case in the  $2^{++}$  glueball.

### 3. The main result on the pole-mass

From the analysis at various temperatures as  $T = 130, 187, 208, 218, 234, 246, 253, 260, 268, 275, 284$  MeV, we plot the SU(3) lattice QCD result for the pole-mass  $m_G(T)$  of the lowest  $0^{++}$  glueball against temperature  $T$  in Fig. 8. The solid circle and the cross denote the thermal glueball mass  $m_G(T)$  obtained with the maximum overlap condition and the mass minimum condition, respectively. We see that they are almost the same. In Fig. 8, we observe a significant pole-mass reduction for the lowest  $0^{++}$  glueball near  $T_c$  as

$$m_G(T) = 1200 \pm 100\text{MeV} \quad \text{for} \quad 0.9T_c < T < T_c, \quad (41)$$

in comparison with  $m_G(T \simeq 0.5T_c) \simeq 1480\text{MeV}$  in our data or  $m_G(T \sim 0) \simeq 1500\text{--}1700$  MeV in the lattice data

in [21, 22, 23]. In this way, we observe nearly 300 MeV reduction or about 20 % reduction of the pole-mass of the lowest  $0^{++}$  glueball in the vicinity of  $T_c$  as

$$m_G(T \sim 0) - m_G(T \simeq T_c) \simeq 300\text{MeV}, \quad (42)$$

$$m_G(T \simeq T_c) \simeq 0.8m_G(T \sim 0).$$

It is remarkable that the pole-mass shift obtained here is much larger than any other pole-mass shifts which has been ever observed in the meson sector in lattice QCD [13, 14].

We next consider the glueball size. To this end, we seek for  $N_{\text{smr}}$ , which realizes the maximum overlap condition. Such  $N_{\text{smr}}$  is listed in Table I for each temperature. By using Eq. (22), we give rough estimates of the thermal glueball sizes  $\rho(T)$  at various temperatures, which are shown in Table I. We find

$$\rho \simeq 0.4\text{fm}, \quad (43)$$

both at low and high temperature below  $T_c$ .

In Table I, we summarize the lowest  $0^{++}$  glueball mass  $m_G(T)$ , the ground-state overlap  $C^{\text{max}}$ , correlated  $\chi^2/N_{\text{DF}}$ , the fit-range  $(t_1, t_2)$ , the normalized overlap  $g(0)$ , the corresponding smearing number  $N_{\text{smr}}$ , the  $0^{++}$  glueball size  $\rho(T)$ , and the number of gauge field configurations  $N_{\text{conf}}$ .

### B. Thermal $2^{++}$ glueball

We show, in Figs. 9 (a) and 10 (a), the  $2^{++}$  glueball correlators  $G(t)/G(0)$  for  $T = 130$  and  $253$  MeV, respectively, after the suitable smearings as Eq. (29). The solid lines denote the results of the best-fit analysis of single-cosh type. The fit-ranges are indicated by the vertical dotted lines, which are determined from the plateaus in the corresponding effective mass plots shown in Figs. 9 (b) and 10 (b).

From Fig. 9 (a), we find  $C \simeq 0.96$  and  $m_G \simeq 2154$  MeV for the  $2^{++}$  glueball in low temperature case  $T = 130$  MeV, which seems consistent with  $m_G = 2000\text{--}2400$  MeV for the  $2^{++}$  glueball at zero temperature [21]. From Fig. 10 (a), we find  $C \simeq 0.90$  and  $m_G \simeq 1996$  MeV for the  $2^{++}$  glueball in the high temperature case  $T = 253$  MeV ( $< T_c$ ).

By combining the results at various temperatures, we plot the pole-mass of the thermal  $2^{++}$  glueball against temperature in Fig. 11. The solid circle and the cross denote the pole-masses of the thermal  $2^{++}$  glueball obtained with the maximum overlap condition and the mass minimum condition, respectively. We see again that they are qualitatively almost the same. The thermal  $2^{++}$  glueball shows a tendency to decline by about 100 MeV for  $T < 0.9T_c$ , which is rather modest in contrast to the  $0^{++}$  glueball. However, in the very vicinity of  $T_c$ , it shows a sudden reduction of about 500 MeV.

In Table II, we summarize the lowest  $2^{++}$  glueball mass  $m_G(T)$ , the ground-state overlap  $C^{\text{max}}$ , correlated

TABLE I: The pole-mass  $m_G(T)$  of the lowest  $0^{++}$  glueball at finite temperature  $T$  in SU(3) lattice QCD. The temperature  $T$ , the temporal lattice size  $N_t$ , the thermal glueball pole-mass  $m_G(T)$ , the maximum ground-state overlap  $C^{\max}$ , the correlated  $\chi^2/N_{\text{DF}}$ , the fit range  $(t_1, t_2)$ , the normalized ground-state overlap  $g(0)$ , the smearing number  $N_{\text{smr}}$ , the thermal glueball size  $\rho(T)$  with Eq. (22), and the number of the gauge configurations  $N_{\text{conf}}$  are listed. The best smearing on  $N_{\text{smr}}$  is determined with maximum overlap condition. Above  $T_c \simeq 280$  MeV, the data such as  $m_G$  is to be understood as the best-fit parameters.

$T$ [MeV]	$N_t$	$m_G$ [MeV]	$C^{\max}$	$\chi^2/N_{\text{DF}}$	$(t_1, t_2)$	$g(0)$	$N_{\text{smr}}$	$\rho$ [fm]	$N_{\text{conf}}$
130	72	1482(25)	0.95(1)	1.60	( 5,14)	0.95(1)	39	0.43	5500
187	50	1436(26)	0.94(1)	0.60	( 5,25)	0.94(1)	41	0.44	5700
208	45	1469(25)	0.96(1)	0.73	( 5,22)	0.96(1)	36	0.41	6400
218	43	1333(34)	0.89(1)	1.22	( 7,21)	0.89(1)	41	0.44	9200
234	40	1288(37)	0.87(2)	1.01	( 8,20)	0.87(2)	36	0.41	8600
246	38	1265(34)	0.88(1)	1.21	( 7,13)	0.88(1)	39	0.43	8900
253	37	1294(26)	0.89(1)	1.45	( 6,17)	0.90(1)	37	0.41	8900
260	36	1158(41)	0.80(2)	1.54	(10,17)	0.81(2)	42	0.44	9900
268	35	1226(30)	0.85(1)	2.74	( 7,11)	0.86(1)	34	0.40	9900
275	34	1174(35)	0.81(2)	0.12	( 9,12)	0.82(2)	44	0.45	9900
284	33	1168(27)	0.82(1)	1.01	( 8,16)	0.83(1)	41	0.44	9900
312	30	1158(28)	0.79(2)	1.22	( 8,15)	0.80(2)	45	0.46	9900
334	28	1091(38)	0.75(2)	1.37	( 8,14)	0.78(2)	44	0.45	6200
360	26	1256(26)	0.84(1)	1.72	( 6,13)	0.87(1)	36	0.41	6800
390	24	1199(33)	0.79(2)	0.88	( 8,12)	0.82(2)	33	0.39	7700

$\chi^2/N_{\text{DF}}$ , the fit-range  $(t_1, t_2)$ , the normalized overlap  $g(0)$ , the corresponding smearing number  $N_{\text{smr}}$ , the  $2^{++}$  glueball size  $\rho(T)$ , and the number of gauge configurations  $N_{\text{conf}}$ .

### C. Glueball correlations above $T_c$

In the deconfinement phase above  $T_c$ , neither hadrons nor glueballs are elementary excitations any more. Instead, quarks and gluons appear as elementary excitations in the quark gluon plasma. Therefore, we might wonder if there is anything interesting in investigating the color-singlet modes such as hadrons and glueballs above  $T_c$ . Nevertheless, based on the lattice-QCD Monte Carlo studies on the screening mass, it was pointed out that some of the strong correlations survive even above  $T_c$  in the scalar and pseudoscalar color-singlet modes such as  $\sigma$  and pions[12]. Hence, at least in the neighborhood of  $T_c$ , it may be possible that some of the nonperturbative effects survive in the deconfinement phase, which provides interesting information of the high-temperature QCD.

In this subsection, we attempt to examine the temporal correlator of the glueball-like color-singlet modes above  $T_c$ . We simply apply the pole-mass analysis of the temporal correlators on the anisotropic lattice with  $N_t = 24, 26, 28, 30, 33$ , which correspond to  $T = 390, 360, 334, 312, 284$  MeV, respectively. (A more sophisticated analysis will be performed in Sect. V.)

We show, in Figs. 12, 13, the temporal correlators  $G(t)/G(0)$  together with the associated effective masses  $m_{\text{eff}}(t)$  at  $T = 312, 390$  MeV, respectively, for the  $0^{++}$  glueball-like color-singlet mode. In each effective-mass plot, a plateau is observed in the region indicated by the vertical dotted lines. By simply applying the single-cosh

fit within the fit-range determined from the plateau, the ‘‘pole-mass’’ of the  $0^{++}$  glueball is extracted above  $T_c$ , which is listed in Table I. We observe that the ‘‘pole-mass’’ is of about 1200 MeV, and that it changes rather continuously across the critical temperature  $T_c$ .

We perform the similar analysis for the  $2^{++}$  glueball-like mode. In Figs. 14 and 15, the temporal correlators  $G(t)/G(0)$  are plotted together with the associated effective mass plots at  $T = 312, 390$  MeV, respectively. In each effective mass plot, we observe a plateau in the region, which is indicated by the vertical dotted lines. Similar to the  $0^{++}$  case, we simply apply the single-cosh fit within the fit-range determined from the plateau to extract the ‘‘pole-mass’’. The results are listed in Table II. We observe that the ‘‘pole-mass’’ is about 1400 MeV, and that its change is again rather continuous across the critical temperature  $T_c$ .

In both of these  $0^{++}$  and  $2^{++}$  cases, the size of the plateau tends to shrink at high temperatures above  $T_c$ . We note that, at much higher temperatures, the plateau finally disappears, which, however, seems to be due to the failure of the ground-state saturation in such a limited temporal size. At any rate, these phenomena suggest that the single-cosh ansatz becomes inappropriate for the fit-function of the temporal correlator  $G(t)$  above  $T_c$  at such a high temperature. However, because of the existence of the plateau in the effective-mass plot, we do not exclude so far the possibility that the color-singlet modes exist as meta-stable modes just above  $T_c$ . According to the lattice data, the color-singlet  $0^{++}$  and  $2^{++}$  modes have the pole-mass of about 1200 MeV and 1400 MeV, respectively, provided that it can be regarded as a bound state. However, even in this case, it should be kept in mind that such glueball-like modes can decay into two or more gluons in the quark-gluon-plasma phase. Since they

TABLE II: The pole-mass  $m_G(T)$  of the lowest  $2^{++}$  glueball at finite temperature  $T$  in SU(3) lattice QCD. The meaning of  $T$ ,  $N_t$ ,  $m_G(T)$ ,  $C^{\max}$ ,  $\chi^2/N_{\text{DF}}$ ,  $(t_1, t_2)$ ,  $g(0)$ ,  $N_{\text{smr}}$ ,  $R$ , and  $N_{\text{conf}}$  are the same as those in Table I. The best smearing on  $N_{\text{smr}}$  is determined with maximum overlap condition.

$T$ [MeV]	$N_t$	$m_G$ [MeV]	$C^{\max}$	$\chi^2/N_{\text{DF}}$	$(t_1, t_2)$	$g(0)$	$N_{\text{smr}}$	$\rho$ [fm]	$N_{\text{conf}}$
130	72	2167(35)	0.97(1)	1.01	( 5,13)	0.97(1)	54	0.50	5500
187	50	2123(39)	0.95(2)	0.57	( 5,13)	0.95(2)	39	0.43	5700
208	45	2054(58)	0.90(3)	1.07	( 7,19)	0.90(3)	47	0.47	6400
218	43	2146(55)	0.91(3)	1.49	( 7,12)	0.91(3)	68	0.56	9200
234	40	1986(72)	0.85(4)	1.03	( 8,14)	0.85(4)	63	0.54	8600
246	38	2142(55)	0.95(3)	0.33	( 6,14)	0.95(3)	41	0.44	8900
253	37	2009(47)	0.90(2)	1.32	( 6,13)	0.90(2)	38	0.42	8900
260	36	1928(46)	0.88(2)	3.12	( 6,12)	0.88(2)	52	0.49	9900
268	35	1975(65)	0.91(4)	2.12	( 8,16)	0.91(4)	44	0.45	9900
275	34	1607(61)	0.69(4)	0.80	( 9,14)	0.69(4)	48	0.47	9900
284	33	1466(78)	0.60(5)	1.51	(11,16)	0.60(5)	51	0.49	9900
312	30	1319(58)	0.61(4)	0.33	(10,15)	0.62(4)	53	0.50	9900
334	28	1408(52)	0.68(3)	1.93	( 8,14)	0.69(3)	47	0.47	6200
360	26	1440(38)	0.75(2)	0.59	( 7,13)	0.76(2)	61	0.53	6800
390	24	1466(55)	0.68(4)	1.47	( 8,12)	0.70(3)	32	0.39	7700

cannot be stable above  $T_c$ , they will acquire finite decay widths. Hence, for more reliable analysis, it is necessary to take into account the effect of such a width, which will be attempted in Sect. V.

#### D. Discussions and remarks

In this subsection, we compare our results of the pole-mass reduction of the thermal glueball with the related lattice QCD results on the screening masses as well as the pole-masses of various hadrons at finite temperature.

We begin with the discussion of the pole-masses of mesons. The pole-masses of various mesons have been measured at finite temperature by using the anisotropic SU(3) lattice QCD at the quenched level in Refs. [13, 14]. From the same pole-mass analysis as ours, they have found that, both for light mesons and for heavy mesons such as the charmonium, the thermal pole-masses are almost unchanged from their zero-temperature values within the error bar below  $T_c$ . This tendency persists even in the vicinity of  $T_c$  as

$$m_{\text{meson}}(T) \simeq m_{\text{meson}}(T=0), \quad \text{for } T \leq T_c. \quad (44)$$

In contrast, with the same pole-mass analysis, the lowest  $0^{++}$  glueball shows the significant pole-mass reduction of about 300MeV in the vicinity of  $T_c$ . Hence, the pole-mass reduction of the thermal  $0^{++}$  glueball may serve as a better pre-critical phenomenon of the QCD phase transition at finite temperature than the pole-mass shifts of the thermal mesons. Thus the thermal glueball may become an interesting particle in the RHIC project in the future.

We next discuss the related results on the screening mass. The screening mass is defined as the reciprocal of the correlation length along the spatial direction. It can also reflect some of the important nonperturbative

features of the QCD vacuum. Hence, it is also an interesting quantity, which may provide a signal of the QCD phase transition. However, unlike the pole-mass, which is considered to be directly measurable as a mass of an elementary excitation at finite temperature, the screening mass is not thought of as a directly measurable quantity in high energy experiments. In the  $0^{++}$  glueball sector, a significant reduction of the screening mass is reported as

$$m_G^{\text{scr}}(T=0.75T_c)/m_G^{\text{scr}}(T \sim 0) = 0.6 \pm 0.1 \quad (45)$$

in SU(3) isotropic lattice QCD with  $\beta_{\text{lat}} = 5.93$  over the lattice of the size  $16^3 \times N_t$  with  $N_t = 4, 6, 8$  at the quenched level [18, 19]. This significant reduction of the screening mass of the glueball would be an indication of the decrease of the nonperturbative nature of the QCD vacuum. In this sense, it seems to be consistent with our results on the significant reduction of the pole-mass of the thermal  $0^{++}$  glueball near the critical temperature  $T_c$ . In contrast to the  $0^{++}$  glueball, in the meson sector, the changes of the screening mass has been found again rather small below  $T_c$  at the quenched level [17].

#### V. NEW ANALYSIS OF TEMPORAL CORRELATIONS —SPECTRAL FUNCTION

In this section, we attempt to generalize the pole-mass analysis given in Sect. IV. Our aim is to analyze our lattice QCD data of the temporal correlator  $G(t)/G(0)$  without assuming the narrowness of the thermal width of the bound-state peak in the spectral function. We first consider the functional form of the new fit-function, which takes into account the effect of the thermal width. We also provide its theoretical background. We then present the numerical results of this new analysis. The section is closed with several comments and cautions.

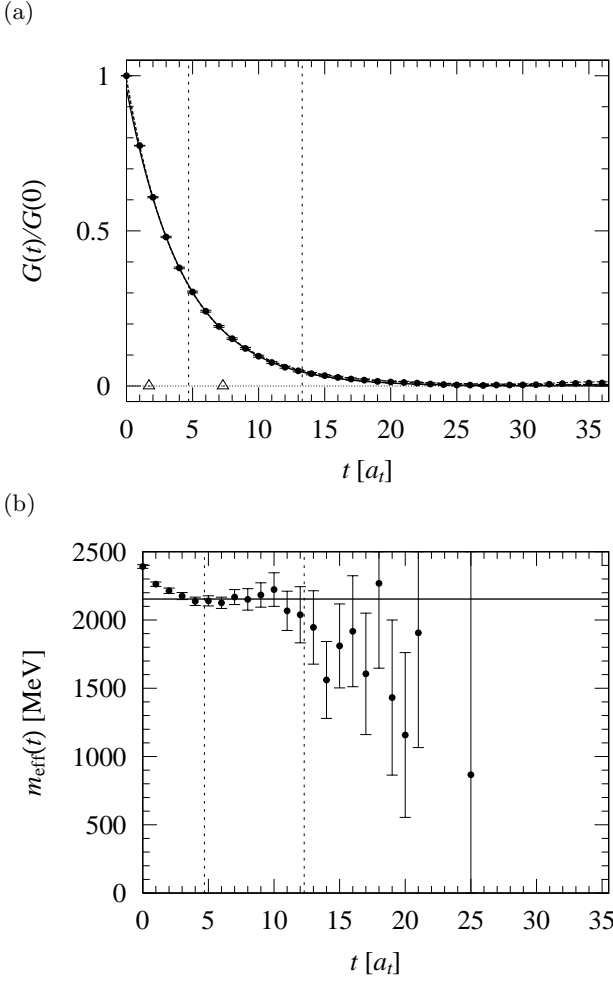


FIG. 9: (a) The  $2^{++}$  glueball correlator  $G(t)/G(0)$  of the at the low temperature ( $T = 130$  MeV). (b) The corresponding cosh-type effective-mass plot. The meaning of the solid lines in both figures and the dashed curve in (a) are the same as in Fig. 5. In (b), the points beyond  $t = 25$  are suppressed due to their huge statistical errors.

#### A. Theoretical consideration on the temporal correlator and the Breit-Wigner fit-function

In Sect. IV, we have presented the results of the pole-masses of the thermal  $0^{++}$  and  $2^{++}$  glueballs at finite temperature obtained in the best-fit analysis of the temporal correlator  $G(t)/G(0)$  with the fit function of the single-cosh type. In this analysis, we have regarded each thermal glueball as a quasi-particle and have assumed that the thermal width of the corresponding peak is sufficiently narrow in the spectral function. In this case, the ground-state contribution to the spectral function can be well approximated as  $\rho(\omega) \simeq 2\pi\{\delta(\omega - m_G(T)) - \delta(\omega + m_G(T))\}$  by introducing the temperature-dependent pole-mass  $m_G(T)$  of the thermal glueball. As a consequence, in order to measure the pole-mass, we can adopt the standard single hyperbolic cosine in Eq. (37) as the fit function, and perform the best-fit analysis in

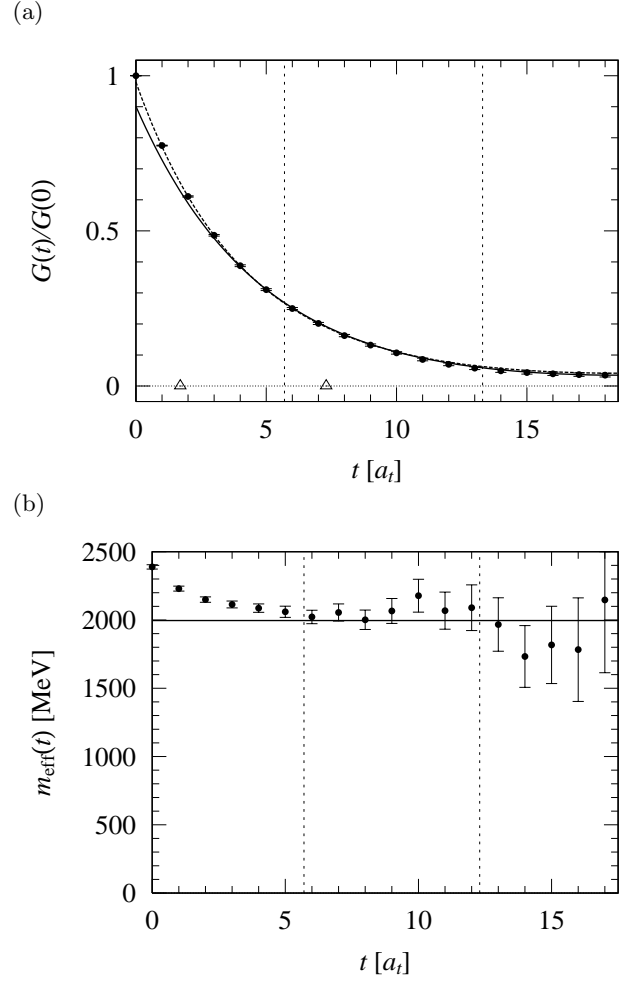


FIG. 10: (a) The  $2^{++}$  glueball correlator  $G(t)/G(0)$  at the high temperature ( $T = 253$  MeV). (b) The corresponding cosh-type effective-mass plot. The meaning of the solid lines in both figures and the dashed curve in (a) are the same as in Fig. 5.

exactly the same way as the zero-temperature case.

However, to be strict, at finite temperature, each bound-state peak in the spectral function  $\rho(\omega)$  acquires a non-zero width through the thermal fluctuations. Since the thermal width would grow with the temperature, it is expected to play the more significant roles and become the less negligible at the higher temperature. Hence, it is desirable to take into account the effect of the thermal width in the best-fit analysis. We can directly see how such a thermal width  $\Gamma(T)$  affects the temporal correlator  $G(t)$  in the spectral representation Eq. (5).

There may have already appeared a signal of such a non-zero thermal width in the glueball correlators in Figs. 5, 6, 12, 13, where the ground-state enhancement works the less effective for the higher temperature. In Table I, we observe a tendency that  $g(0)$  declines with the increasing temperature. For instance,  $g(0) \simeq 0.95$  for the low temperature  $T = 130$  MeV becomes  $g(0) \lesssim 0.90$  for the higher temperature  $T \gtrsim 250$  MeV for the  $0^{++}$

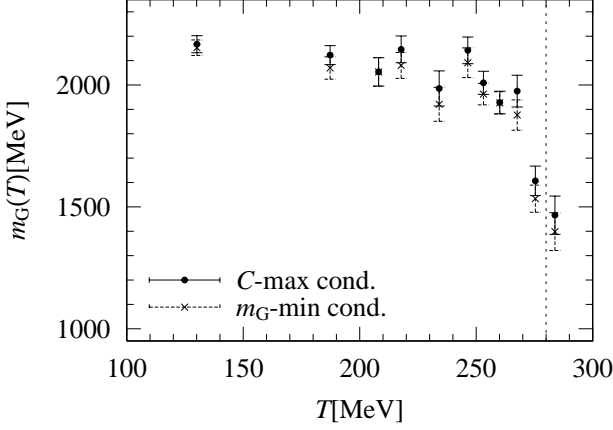


FIG. 11: The  $2^{++}$  glueball mass plotted against temperature  $T$ . The solid circle and the cross denote the thermal  $2^{++}$  glueball mass obtained with the maximum overlap condition and the mass minimum condition, respectively. The vertical dotted line indicates the critical temperature  $T_c \simeq 280$  MeV in quenched QCD.

glueball. In the effective-mass plots in Figs. 5, 6, 12, we observe that the plateau tends to start with the larger  $t$  at the higher temperature. These phenomena may indicate that the existence of the other spectral components become the less negligible at the higher temperature.

In fact, at finite temperature, each bound state peak acquires a thermal width. The thermal width is one of the most feasible candidates for the source of these other spectral components, since the contributions from such a bunch of spectral components cannot be well separated even by means of the smearing procedure. In this section, we perform a more general new analysis of the temporal correlator  $G(t)/G(0)$  as an attempt to take into account the effects of the thermal width  $\Gamma(T)$  of the ground-state peak in the spectral function  $\rho(\omega)$ .

At zero temperature, the bound-state poles of the Green functions  $G_R(\omega)$  and  $G_A(\omega)$  in Eq. (8) lie on the real axis in the complex  $\omega$ -plane. Hence, the lowest-state contribution to the spectral function  $\rho(\omega)$  is expressed as  $\rho(\omega) = 2\pi A \{\delta(\omega - m_G) - \delta(\omega + m_G)\}$ , where  $A$  and  $m_G$  are the strength and the mass of the lowest-state pole, respectively. By inserting this expression into Eq. (5), and taking the limit  $\beta = 1/T \rightarrow \infty$ , we recover the familiar expression as

$$G(t) = \lim_{\beta \rightarrow \infty} A \frac{\cosh(m_G(\beta/2 - t))}{\sinh(\beta m_G/2)} = A e^{-m_G t}. \quad (46)$$

With the increasing temperature, these bound-state poles are moving off the real axis into the second Riemannian sheet of the complex  $\omega$ -plane. Suppose that the ground-state pole is located at  $\omega = \omega_0 - i\Gamma$  ( $\omega_0, \Gamma \in \mathbb{R}$ ) in the second Riemannian sheet. Since the spectral function  $\rho(\omega)$  is the imaginary part of the Green function, the ground-state contribution in the spectral function  $\rho(\omega)$

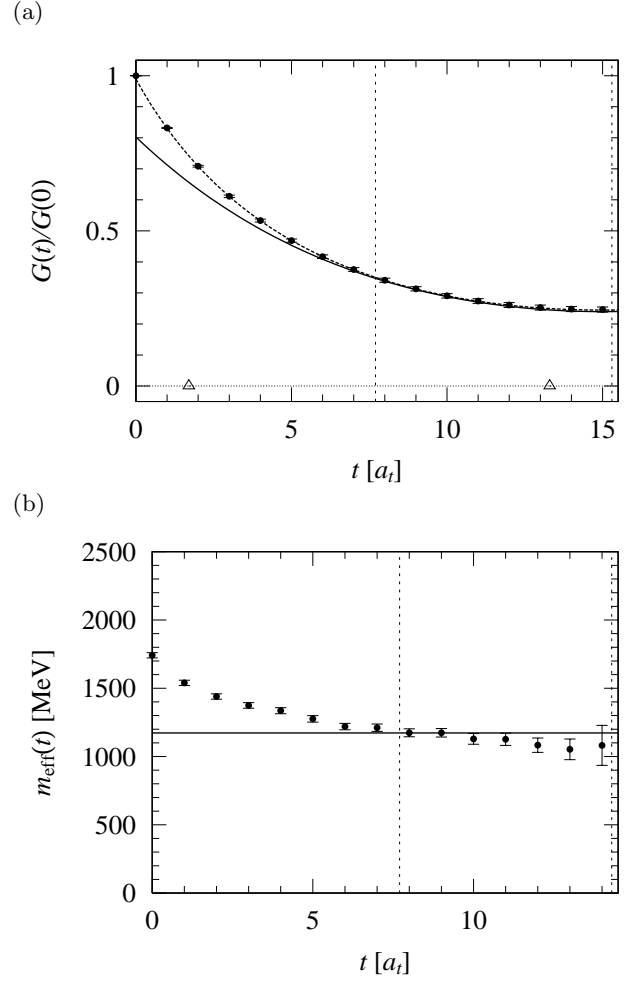


FIG. 12: (a) The  $0^{++}$  glueball correlator  $G(t)/G(0)$  at  $T = 312$  MeV above  $T_c$ . (b) The corresponding cosh-type effective-mass plot. The meaning of the solid lines in both figures and the dashed curve in (a) are the same as in Fig. 5.

can be expressed in the following way:

$$\begin{aligned} \rho(\omega) &= -2\text{Im}(G_R(\omega)) \\ &= 2\pi A \left( \delta_\Gamma(\omega - \omega_0) - \delta_\Gamma(\omega + \omega_0) \right) + \dots \end{aligned} \quad (47)$$

Here,  $A$  represents the residue of the pole,  $\delta_\epsilon(x)$  denotes the Lorentzian at  $x = 0$  with the width  $\epsilon (> 0)$ , which is defined as

$$\delta_\epsilon(x) \equiv \frac{1}{\pi} \text{Im} \left( \frac{1}{x - i\epsilon} \right) = \frac{1}{\pi} \frac{\epsilon}{x^2 + \epsilon^2}. \quad (48)$$

The appearance of the second term in Eq. (47) is due to the fact that the spectral function  $\rho(\omega)$  is an odd function in  $\omega$ , reflecting the bosonic nature of the glueball. “...” in Eq. (47) represents the contributions from the excited states, which are expected to be suppressed after the appropriate smearing procedure. Corresponding to Eq. (47), the ground state contribution in the temporal



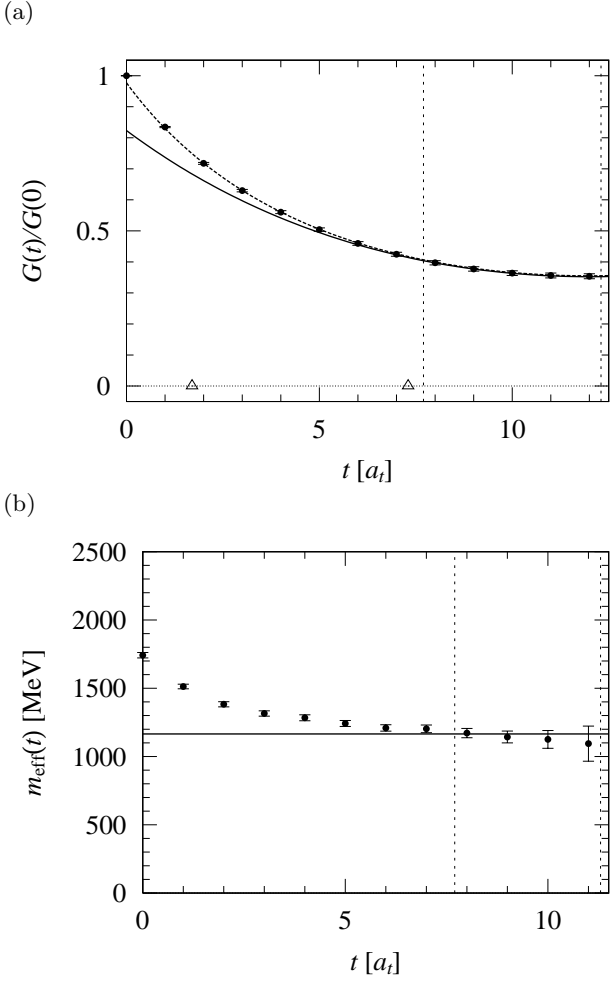


FIG. 13: (a) The  $0^{++}$  glueball correlator  $G(t)/G(0)$  at  $T = 390$  MeV above  $T_c$ . (b) The corresponding cosh-type effective-mass plot. The meaning of the solid lines in both figures and the dashed curve in (a) are the same as in Fig. 5.

glueball correlator  $G(t)$  is expressed as

$$G(t) = \int_{-\infty}^{\infty} \frac{d\omega}{2\pi} \frac{\cosh(\omega(\beta/2 - t))}{\sinh(\beta\omega/2)} \times 2\pi A \left( \delta_{\Gamma}(\omega - \omega_0) - \delta_{\Gamma}(\omega + \omega_0) \right) + \dots \quad (49)$$

Hence, to extract the center  $\omega_0(T)$  and the thermal width  $\Gamma(T)$  of the lowest-state peak in  $G(t)/G(0)$ , the appropriate fit-function is given as

$$g_{\Gamma}(t) \equiv \int_{-\infty}^{\infty} \frac{d\omega}{2\pi} \frac{\cosh(\omega(\beta/2 - t))}{\sinh(\beta\omega/2)} \times 2\pi \tilde{A} \left( \delta_{\Gamma}(\omega - \omega_0) - \delta_{\Gamma}(\omega + \omega_0) \right), \quad (50)$$

where  $\tilde{A}$ ,  $\omega_0$  and the  $\Gamma$  are used as the fit parameters. Here,  $\tilde{A}$  corresponds to  $A/G(0)$  in Eq. (49), and will be referred to as the strength parameter. We will refer to

Eq. (50) as the fit-function of “Breit-Wigner” type. Note that  $g_{\Gamma}(t)$  is a generalization of the fit-function  $g(t)$  of the (a)

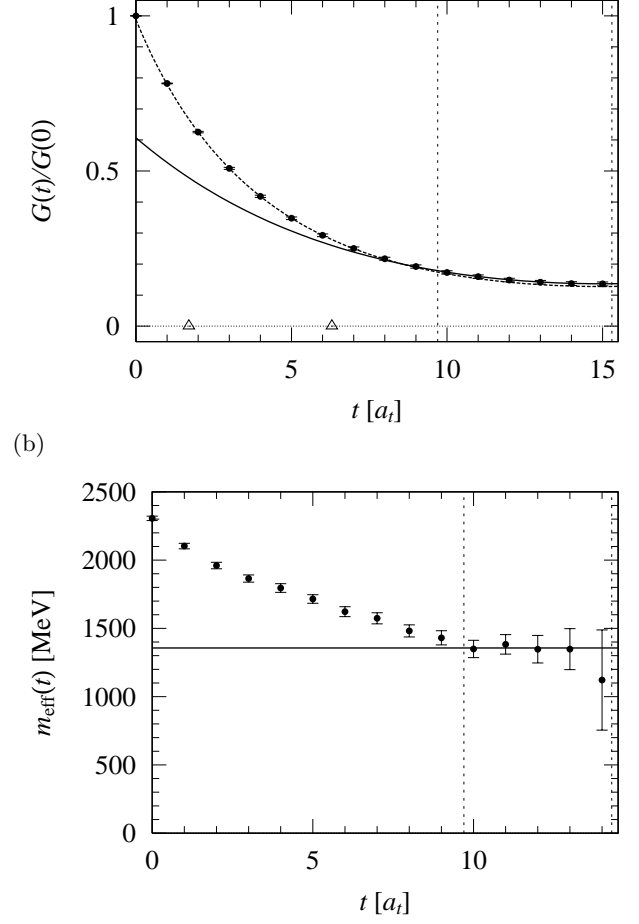


FIG. 14: (a) The  $2^{++}$  glueball correlator  $G(t)/G(0)$  at  $T = 312$  MeV above  $T_c$ . (b) The corresponding cosh-type effective-mass plot. The meaning of the solid lines in both figures and the dashed curve in (a) are the same as in Fig. 5.

single-cosh type in the sense that  $g_{\Gamma}(t)$  reduces to  $g(t)$  in a special limit as

$$\lim_{\Gamma \rightarrow +0} g_{\Gamma}(t) = g(t). \quad (51)$$

In this sense, the best-fit analysis of Breit-Wigner type serves as a generalization of the ordinary pole-mass analysis of single-cosh type. Note that the analysis of Breit-Wigner type is rather general, which is also applicable to the analysis of temporal correlators of various thermal hadrons.

We note that, after some calculations, the fit-function  $g_{\Gamma}(t)$  in Eq. (50) can be expressed by the infinite series as

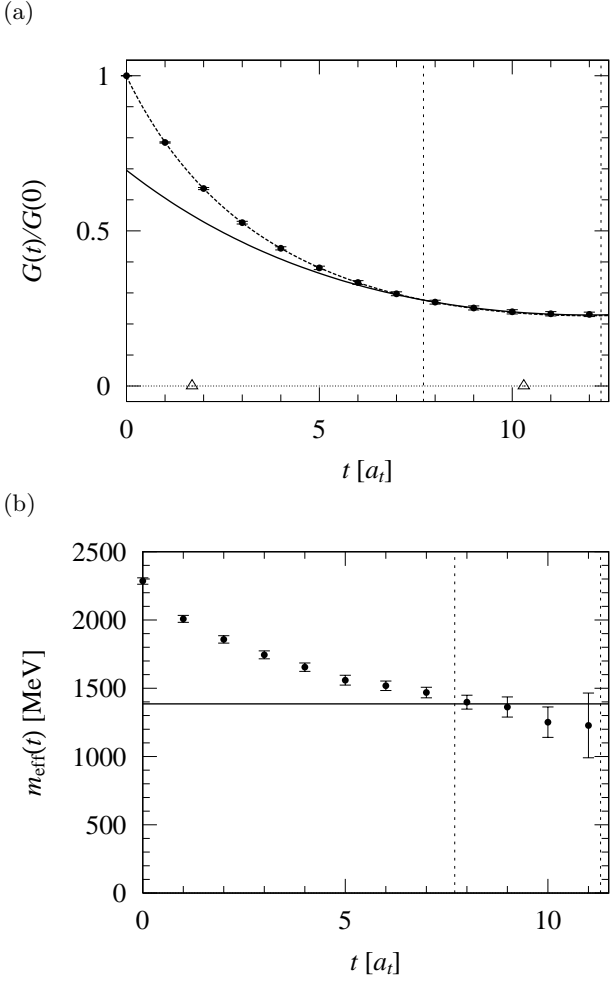


FIG. 15: (a) The  $2^{++}$  glueball correlator  $G(t)/G(0)$  at  $T = 390$  MeV above  $T_c$ . (b) The corresponding cosh-type effective-mass plot. The meaning of the solid lines in both figures and the dashed curve in (a) are the same as in Fig. 5.

$$g_{\Gamma}(t) = \tilde{A} \left[ \text{Re} \left( \frac{\cosh \{(\omega_0 + i\Gamma)t\}}{\sinh \left\{ \frac{\beta}{2}(\omega_0 + i\Gamma) \right\}} \right) + 2\beta\omega_0 \sum_{n=1}^{\infty} \cos \left( \frac{2\pi n}{\beta} t \right) \left\{ \frac{1}{(2\pi n + \beta\Gamma)^2 + \beta^2\omega_0^2} - (n \rightarrow -n) \right\} \right] \quad (52)$$

We make a comment on the role of the smearing method in the presence of the non-zero width of the lowest state (or the ground state) at finite temperature. As was explained in Sect. II, the smearing method aims at a suitable choice of the glueball operators, by providing a series of operators with different quantum sizes, all of which, however, hold the identical quantum numbers in common. Whereas the residues of the bound-state poles are affected by the different choices of the glueball operators, their positions in the complex  $\omega$ -plane are not affected. One can thereby enhance the residue of the particular bound-state pole by a clever choice of the operator, while

keeping its position unaffected. Note that the position of the pole determines the characteristics of the peak, i.e., the center and the width. As this clever choice of the operator, we will use the smearing method, which is expected to pick up and then to enhance the contribution of the ground-state peak.

## B. Setup for the Breit-Wigner fit analysis

In this subsection, we consider the fit-range of the Breit-Wigner fit analysis for the temporal glueball cor-

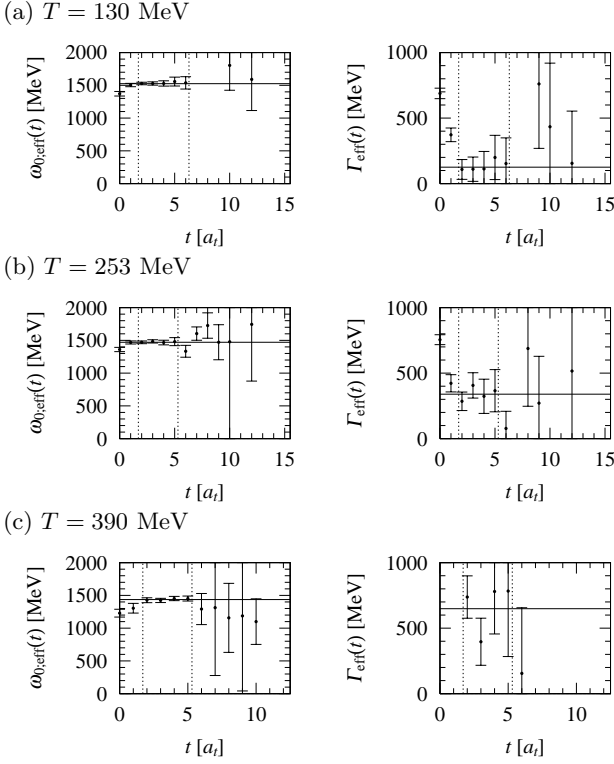


FIG. 16: The effective center  $\omega_{0,\text{eff}}(t)$  and the effective width  $\Gamma_{\text{eff}}(t)$  of the  $0^{++}$  glueball correlator at various temperatures (a)  $T = 130$  MeV, (b)  $T = 253$  MeV and (c)  $T = 390$  MeV. The solid lines represents the results of the best-fit analysis of Breit-Wigner type. Here, the fit-ranges are determined from the simultaneous plateaus, which are indicated with the vertical dotted lines.

relator  $G(t)$ . We examine also the  $N_{\text{smr}}$ -dependence of the best-fit parameters in order to estimate the systematic error originating from a particular choice of  $N_{\text{smr}}$ .

### 1. The fit range

We consider the determination of the fit-range of the Breit-Wigner fit analysis. As a consequence of the smearing method, the contribution from the ground-state peak is expected to be enhanced in the spectral function  $\rho(\omega)$ . However, even with the smearing method, the complete elimination of all the excited-state contributions is practically impossible. Therefore, we have to reduce further the remaining contributions from the higher spectral components as much as possible. To this end, we seek for the appropriate fit-range, where  $G(t)$  consists of nearly a single-peak contribution. We adopt the strategy, which is a straightforward extension to the one adopted in the single-cosh analysis, i.e., the analysis based on the effective-mass plot in the following way. We consider the “effective center”  $\omega_{0,\text{eff}}(t)$  and the “effective width”  $\Gamma_{\text{eff}}(t)$ , which are defined as the solutions to the following

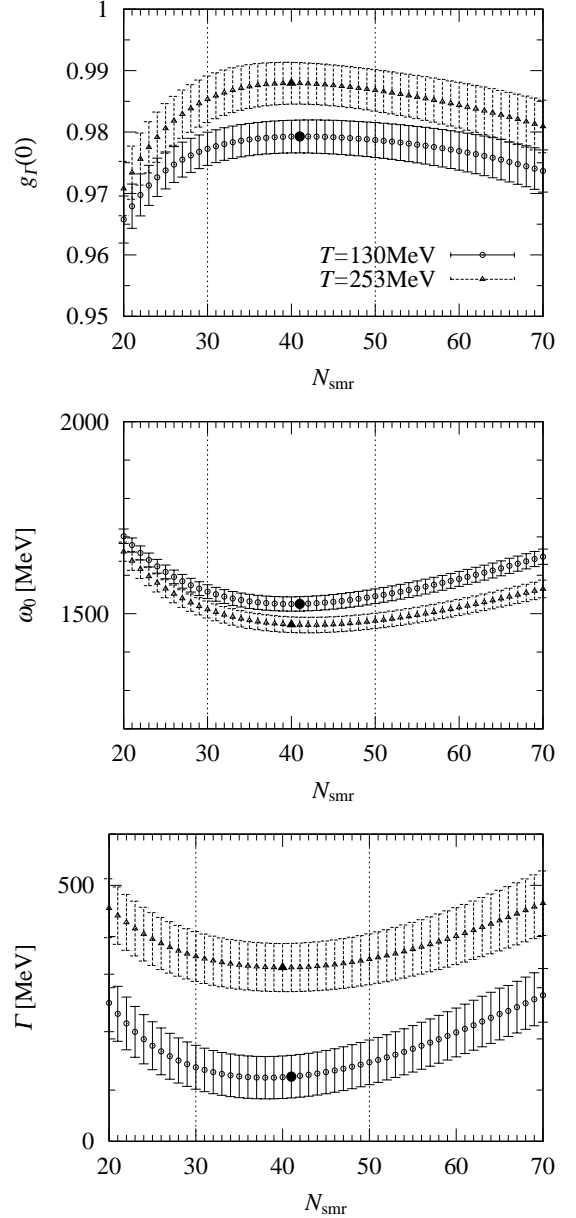


FIG. 17: The normalized overlap  $g_{\Gamma}(0)$ , the center  $\omega_0$  and the thermal width  $\Gamma$  of the lowest peak of the  $0^{++}$  glueball against the smearing number  $N_{\text{smr}}$  in the confinement phase at  $T = 130$  MeV and 250 MeV, which are denoted by the circle and the triangle, respectively. The solid symbols denote the data where  $g_{\Gamma}(0)$  becomes maximum. Both for  $\omega_0$  and  $\Gamma$ , the  $N_{\text{smr}}$ -dependence is small in the region of  $30 \leq N_{\text{smr}} \leq 50$ .

equations:

$$\begin{aligned} G(t)/G(t+1) &= g_{\Gamma}(t)/g_{\Gamma}(t+1) \\ G(t+1)/G(t+2) &= g_{\Gamma}(t+1)/g_{\Gamma}(t+2), \end{aligned} \quad (53)$$

for given  $G(t)/G(t+1)$  and  $G(t+1)/G(t+2)$  at each fixed  $t$ . In Fig. 16, we show the plots of the effective centers  $\omega_{0,\text{eff}}(t)$  and the effective width  $\Gamma_{\text{eff}}(t)$  of the  $0^{++}$  glueball correlators at various temperatures  $T = 130, 253, 390$

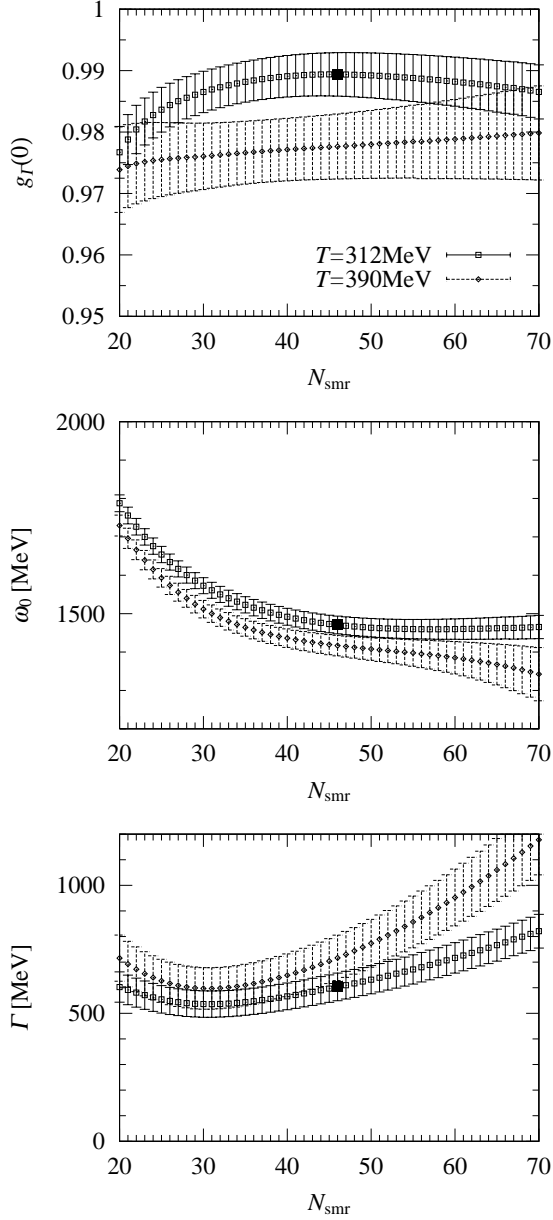


FIG. 18: The similar figure as Fig. 17 in the deconfinement phase at  $T = 312$  MeV and  $390$  MeV, denoted by the square and diamond, respectively. The absence of the solid diamond is due to the missing maximum of the normalized overlap  $g_r(0)$  in the region  $N_{\text{smr}} < 70$ .

MeV. The statistical errors for  $\omega_{0;\text{eff}}(t)$  and  $\Gamma_{\text{eff}}(t)$  are estimated with the jackknife analysis. In each pair of  $\omega_{0;\text{eff}}(t)$  and  $\Gamma_{\text{eff}}(t)$  plots, there appears a simultaneous plateau, a region where  $\omega_{0;\text{eff}}(t)$  and  $\Gamma_{\text{eff}}(t)$  are almost constant simultaneously. In this region,  $G(t)$  is expected to consist of a single peak contribution, and  $g_r(t)$  can properly represent the contribution of the ground-state peak in Eq. (49). Note that a nontrivial  $t$ -dependence indicates the existence of the contributions from the other spectral components. In this sense, the existence

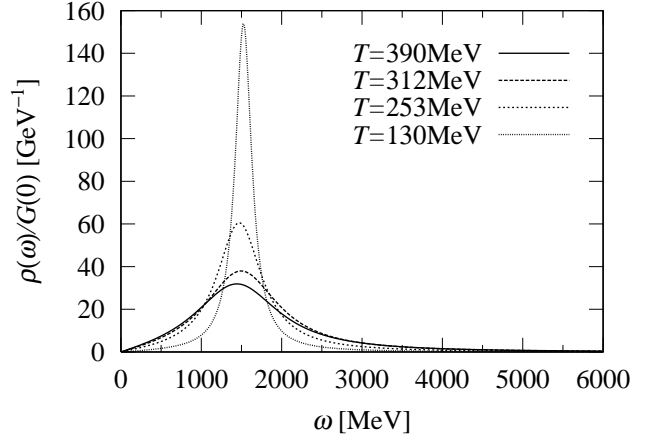


FIG. 19: The spectral function  $\rho(\omega)$  of the lowest  $0^{++}$  glueball at  $T = 130, 253, 312, 390$  MeV, obtained from the Breit-Wigner fit analysis of the  $0^{++}$ -glueball temporal correlator  $G(t)/G(t)$ .

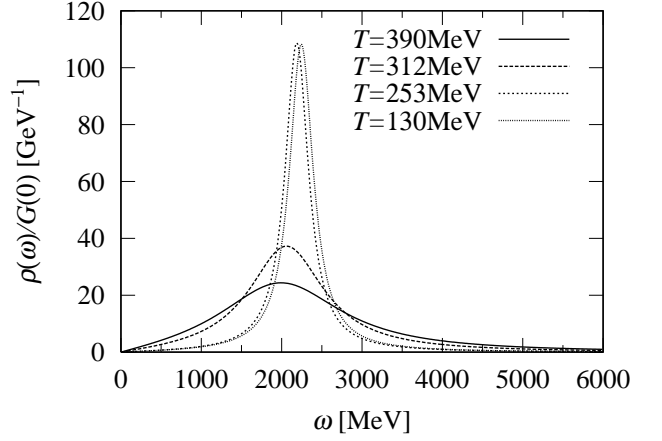


FIG. 20: The spectral function  $\rho(\omega)$  of the lowest  $2^{++}$  glueball at  $T = 130, 253, 312, 390$  MeV, obtained from the Breit-Wigner fit analysis of the  $2^{++}$ -glueball temporal correlator  $G(t)/G(t)$ .

of the simultaneous plateau in the pair of  $\omega_{0;\text{eff}}(t)$  and  $\Gamma_{\text{eff}}(t)$  plots works as a necessary condition to determine whether the fit function  $g_r(t)$  of Breit-Wigner type is appropriate or not.

## 2. The $N_{\text{smr}}$ dependence

We consider the  $N_{\text{smr}}$ -dependences of the best-fit parameters, the center  $\omega_0(T)$  and the thermal width  $\Gamma(T)$  of the lowest peak. Since the physical meaning of  $\tilde{A}$  is not so obvious in the presence of the thermal width, we consider  $g_r(0)$  instead of  $\tilde{A}$ . Note that  $g_r(0)$  is a generalization of  $g(0)$  in the single-cosh analysis. We will refer to  $g_r(0)$  as the “(normalized) overlap” with the state corresponding to the lowest peak.

TABLE III: The analysis of the temporal correlator  $G(t)/G(0)$  of the thermal  $0^{++}$  glueball based on Breit-Wigner ansatz of the spectral function  $\rho(\omega)$  as Eq. (47). The temperature  $T$ , the temporal lattice size  $N_t$ , the center  $\omega_0$ , the width  $\Gamma$  and the strength parameter  $\tilde{A}$  of the peak, the correlated  $\chi^2/N_{\text{DF}}$ , the fit-range  $(t_1, t_2)$ , the overlap  $g_\Gamma(0)$ , the smearing number  $N_{\text{smr}}$  which achieves the  $g_\Gamma(0)$ -max condition, and the gauge configuration number  $N_{\text{conf}}$  are listed. The asterisk “\*” in the column of  $N_{\text{smr}}$  indicates that the original value of  $N_{\text{smr}}$  is 70, which had been replaced by the suitable smearing number 40. We had done this, because  $N_{\text{smr}} = 70$  is the end point and because the situation similar to the one in Fig. 18 at  $T = 390$  is observed.

$T$ [MeV]	$N_t$	$\omega_0$ [MeV]	$\Gamma$ [MeV]	$\tilde{A}$	$\chi^2/N_{\text{DF}}$	$(t_1, t_2)$	$g_\Gamma(0)$	$N_{\text{smr}}$	$N_{\text{conf}}$
130	72	1525(19)	126( 42)	1.03( 2)	0.14	(2, 8)	0.979(3)	41	5500
187	50	1532(20)	165( 42)	1.04( 2)	0.65	(2,16)	0.977(3)	34	5700
208	45	1548(22)	165( 45)	1.05( 2)	1.48	(2, 9)	0.985(3)	33	6400
218	43	1547(22)	302( 55)	1.11( 3)	0.94	(3, 8)	0.992(6)	31	9200
234	40	1476(21)	279( 48)	1.09( 2)	1.23	(2, 6)	0.988(3)	42	8600
246	38	1467(22)	323( 46)	1.11( 2)	0.37	(2, 9)	0.990(3)	37	8900
253	37	1471(20)	339( 47)	1.11( 2)	0.53	(2, 7)	0.988(3)	40	8900
260	36	1418(26)	284( 50)	1.07( 3)	0.18	(3,10)	0.976(5)	42	9900
268	35	1468(22)	392( 48)	1.13( 3)	0.36	(2, 8)	0.989(3)	35	9900
275	34	1486(27)	357( 69)	1.10( 4)	2.04	(3, 8)	0.980(8)	32	9900
284	33	1432(19)	484( 52)	1.17( 3)	1.89	(2,10)	0.988(3)	45	9900
312	30	1471(23)	603( 54)	1.21( 3)	1.40	(2,13)	0.989(4)	46	9900
334	28	1437(38)	795( 85)	1.32( 6)	1.00	(2,12)	0.997(5)	43	6200
360	26	1489(34)	740(104)	1.25( 7)	0.83	(2, 6)	0.992(6)	36	6800
390	24	1436(24)	648( 84)	1.16( 5)	1.00	(2, 7)	0.977(5)	40*	7700

TABLE IV: The analysis of the thermal  $2^{++}$  glueball correlator  $G(t)/G(0)$  with Breit-Wigner ansatz of the spectral function  $\rho(\omega)$ . The meaning of  $T$ ,  $N_t$ ,  $\omega_0$ ,  $\Gamma$ ,  $\tilde{A}$ ,  $\chi^2/N_{\text{DF}}$ ,  $(t_1, t_2)$ ,  $g_\Gamma(0)$  and  $N_{\text{conf}}$  are the same as those in Table III.

$T$ [MeV]	$N_t$	$\omega_0$ [MeV]	$\Gamma$ [MeV]	$\tilde{A}$	$\chi^2/N_{\text{DF}}$	$(t_1, t_2)$	$g_\Gamma(0)$	$N_{\text{smr}}$	$N_{\text{conf}}$
130	72	2250(21)	182( 60)	1.04( 2)	1.23	(2, 7)	0.989(5)	39	5500
187	50	2182(28)	131( 70)	1.02( 3)	0.59	(2,10)	0.980(7)	48	5700
208	45	2233(26)	148( 76)	1.02( 3)	1.21	(2, 6)	0.983(7)	47	6400
218	43	2224(21)	88( 44)	1.00( 2)	1.42	(2,10)	0.978(4)	49	9200
234	40	2270(42)	192( 83)	1.05( 4)	0.20	(3, 7)	0.998(12)	38	8600
246	38	2242(24)	126( 56)	1.02( 2)	1.40	(2,18)	0.983(5)	58	8900
253	37	2174(25)	202( 56)	1.04( 2)	0.10	(2, 7)	0.981(5)	54	8900
260	36	2169(23)	255( 59)	1.05( 2)	0.46	(2, 8)	0.983(6)	41	9900
268	35	2164(24)	334( 68)	1.08( 3)	1.24	(2, 7)	0.987(6)	55	9900
275	34	2173(22)	306( 58)	1.06( 2)	1.54	(2, 8)	0.980(5)	40*	9900
284	33	2123(24)	523( 66)	1.15( 3)	0.16	(2, 7)	0.997(5)	55	9900
312	30	2058(26)	571( 75)	1.16( 3)	0.48	(2, 6)	0.988(6)	40*	9900
334	28	2011(33)	839(116)	1.28( 6)	0.26	(2, 6)	1.002(8)	51	6200
360	26	1943(32)	922(109)	1.31( 6)	0.03	(2, 7)	1.001(8)	52	6800
390	24	1981(33)	940(111)	1.29( 6)	0.41	(2,10)	0.998(8)	40*	7700

In Fig. 17, the normalized overlap  $g_\Gamma(0)$ , the center  $\omega_0(T)$  and the thermal width  $\Gamma(T)$  are plotted against  $N_{\text{smr}}$  for fixed  $\alpha = 2.1$  at  $T = 130$  and 253 MeV below  $T_c$  with circles and triangles, respectively. In the region of  $30 \leq N_{\text{smr}} \leq 50$ ,  $g_\Gamma(0)$  is maximized, and  $\omega_0(T)$  and  $\Gamma(T)$  are minimized. These behaviors of  $g_\Gamma(0)$  and  $\omega_0(T)$  are analogous to those of the normalized overlap  $g(0)$  (or the overlap  $C$ ) and the pole-mass  $m_G(T)$  in the single-cosh analysis. As for the thermal width  $\Gamma(T)$ , since the contamination of the higher spectral components is expected to make it wider, the minimal  $\Gamma(T)$  would characterize the lowest-peak saturation.

According to these considerations, we expect that the lowest-peak contribution is maximally enhanced in the

region of  $30 \leq N_{\text{smr}} \leq 50$ , and that the normalized overlap  $g_\Gamma(0) \simeq 1$  provides a saturation rate of the lowest-peak contribution, in exactly the same way as  $g(0) \simeq 1$  does in the single-cosh analysis. Note that both for the center  $\omega_0$  and the thermal width  $\Gamma$ , the  $N_{\text{smr}}$ -dependence is rather small in the region of  $30 \leq N_{\text{smr}} \leq 50$ , resulting in the small systematic error on the specific choice of  $N_{\text{smr}}$ . The behaviors are qualitatively the same at the other temperatures below  $T_c$ . This is also the case for the  $2^{++}$  glueball.

In contrast, qualitatively different behaviors appear above  $T_c$ . In Fig. 18, the normalized overlap  $g_\Gamma(0)$ , the center  $\omega_0$  and the thermal width  $\Gamma$  are plotted against  $N_{\text{smr}}$  for  $\alpha = 2.1$  at  $T = 312$  and 390 MeV above  $T_c$

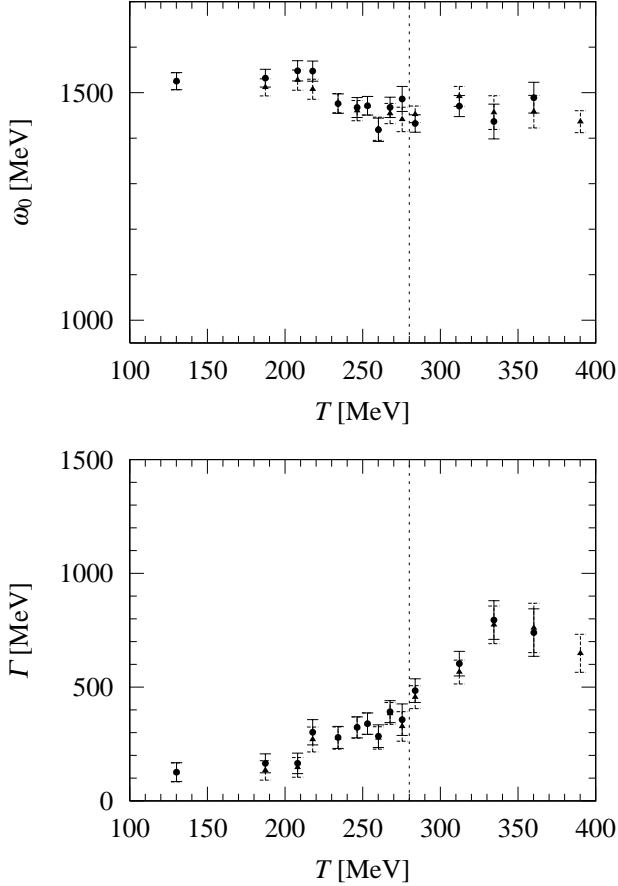


FIG. 21: The center  $\omega_0(T)$  and the width  $\Gamma(T)$  of the lowest-state peak in the spectral function  $\rho(\omega)$  for the  $0^{++}$  glueball against temperature  $T$  in the Breit-Wigner fit analysis. The triangle denotes the results associated with the suitable smearing as Eq. (29), and the circle denote the results with  $N_{\text{smr}}$  listed in Table III, which maximizes the normalized overlap  $g_{\Gamma}(0)$ .

with the square and the diamond, respectively. We see that the overlap  $g_{\Gamma}(0)$  becomes too insensitive to  $N_{\text{smr}}$  to determine its maximum. In some cases, it does not take the maximum in the region  $N_{\text{smr}} < 70$ . In addition, there are sizable  $N_{\text{smr}}$ -dependences in  $\omega_0$  and  $\Gamma$  in this region, although  $\Gamma$  seem to take its minimum around the typical smearing number as  $N_{\text{smr}} \sim 40$ . As for the center  $\omega_0$ , it continues to decline and does not take the minimum in the region  $N_{\text{smr}} < 70$ . We note that qualitatively the same behaviors are observed in the  $2^{++}$  channel. Considering these behaviors, it would be better to consider the Breit-Wigner analysis both in the case with  $N_{\text{smr}} = 40$  and in the case with  $N_{\text{smr}}$  which maximizes  $g_{\Gamma}(0)$  above  $T_c$ .

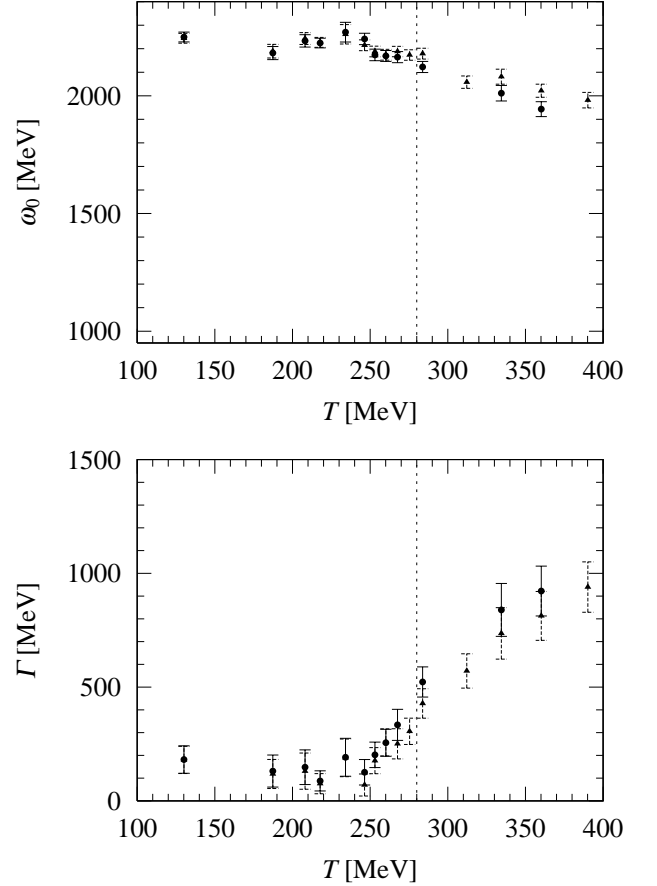


FIG. 22: The center  $\omega_0(T)$  and the width  $\Gamma(T)$  of the lowest-state peak in the spectral function  $\rho(\omega)$  for the  $2^{++}$  glueball against temperature  $T$  in the Breit-Wigner fit analysis. The triangle denotes the results in the suitable smearing as Eq. (29), and the circle denote the results with  $N_{\text{smr}}$  listed in Table IV, which maximizes the normalized overlap  $g_{\Gamma}(0)$ .

### 3. The smearing and the single-pole saturation

In this section, we use the smearing method to enhance the residues of the pair of the complex poles associated with the low-lying peak. However, in the presence of the non-zero thermal width, the meaning of the “low-lying” contribution may become less definite in a strict sense, since these peaks can overlap with each other. With the increasing temperature, the thermal width becomes wider. Hence, each bound-state peak becomes less distinguishable from one another due to the possibly strong overlap with the neighboring peaks. In some cases, one may wonder if the smearing really extract only the contribution from the lowest-state peak among the overlapping peaks. Therefore, we have to check the smallness of the excited-state contamination by examining the quality of the fitting of  $G(t)/G(0)$  with  $g_{\Gamma}(t)$ . If  $G(t)/G(0)$  can be well fitted with  $g_{\Gamma}(t)$  corresponding to the single Lorentzian peak, we may expect that the lowest-state

dominates in the spectral function  $\rho(\omega)$  as a result of the smearing.

### C. Numerical results of the Breit-Wigner fit

In this subsection, we perform the Breit-Wigner fit analysis for the lattice QCD data of the temporal glueball correlator. We also present the numerical results on the spectral function of the glueballs at various temperatures.

#### 1. The glueball correlators and the spectral functions

In Figs. 5 (a), 6 (a), 12 (a), 13 (a), we show the best-fit function  $g_\Gamma(t)$  for the  $0^{++}$  glueball correlator  $G(t)/G(0)$  with dashed curves at various temperatures as  $T = 130, 253, 312, 390$  MeV, respectively. Similarly for the  $2^{++}$  glueball, in Figs. 9 (a), 10 (a), 14 (a), 15 (a), the best-fit functions  $g_\Gamma(t)$  are added with dashed curves at various temperatures as  $T = 130, 253, 312, 390$  MeV, respectively. It is remarkable that, at all of these temperatures, the lattice QCD data of the temporal glueball correlators  $G(t)/G(0)$  are in a good agreement with  $g_\Gamma(t)$  in the whole region of  $t$ .

In Figs. 19 and 20, we plot the spectral functions  $\rho(\omega)$  in the  $0^{++}$  and  $2^{++}$  glueball channels at various temperatures. In both the channels, we observe the tendency that the thermal width grows with the increasing temperature (up to the statistical errors). To be strict, each of these curves corresponds to actually a part of the spectral function  $\rho(\omega)$ , i.e., it is the ground-state contribution in the spectral function rather than the original spectral function itself. This can be understood in the following way. Recall that the best-fit analysis is performed in the fit-range determined from the simultaneous plateau in the plots of the effective center  $\omega_{0;\text{eff}}(t)$  and the effective width  $\Gamma_{\text{eff}}(t)$ . In this fit-range,  $G(t)$  is expected to be less sensitive to the existence of the higher spectral components, and hence, it becomes possible to extract only the contribution from the ground-state peak. However, in order to express  $G(t)$  with the spectral function  $\rho(\omega)$  (cf. Eq. (5)) in the whole region of  $t$ , the higher spectral components should be necessary even after the smearing procedure is applied. Nevertheless, the goodness of the fitting in Figs. 5, 6, 12, 13, 9, 10, 14 and 15 indicates that the contributions from the higher spectral components may be actually rather small.

#### 2. The main result of the Breit-Wigner fit

In Fig. 21, the center  $\omega_0(T)$  and the thermal width  $\Gamma(T)$  of the lowest-state peak of the spectral function  $\rho(\omega)$  in the  $0^{++}$  glueball channel are plotted against temperature  $T$ . Here, the triangles denote the results for the suitable smearing with  $N_{\text{smr}} = 40$ , and the circles denote

the results with  $N_{\text{smr}}$ , which maximizes the normalized overlap  $g_\Gamma(0)$ . The agreement of both results indicates that the systematic error originating from the particular choice of  $N_{\text{smr}}$  is small.

We observe that the thermal width  $\Gamma(T)$  grows gradually with the increasing temperature, resulting in the significant increase near the critical temperature  $T_c$  as

$$\Gamma(T \sim T_c) \sim 300\text{MeV}. \quad (54)$$

The center  $\omega_0(T)$  is observed to decline modestly by about 100 MeV near  $T_c$  as  $\omega_0(T \sim T_c) \simeq 1440$  MeV in comparison with  $\omega_0(T \sim 0) \simeq 1530$  MeV.

In Fig. 22, the center  $\omega_0(T)$  and the thermal width  $\Gamma(T)$  of the lowest-state peak of the spectral function  $\rho(\omega)$  in the  $2^{++}$  glueball channel are plotted against temperature  $T$ . In comparison with the  $0^{++}$  glueball case, changes are observed less significant in the  $2^{++}$  glueball channel below  $T_c$ , which, however, is followed by a sudden expansion of the thermal width  $\Gamma(T)$  around  $T \sim T_c$ . This sudden expansion of  $\Gamma(T)$  may indicate the instability of the thermal  $2^{++}$  glueball around  $T_c$ .

In Tables III and IV, we summarize the results of the Breit-Wigner fit analysis for the  $0^{++}$  and the  $2^{++}$  glueballs, respectively, such as the center  $\omega_0(T)$ , the thermal width  $\Gamma(T)$  and the strength parameter  $A$  of the lowest-state peak, which play the role of the fit parameters, and so on.

As a remarkable result of the Breit-Wigner analysis, we emphasize that the gradual growth of the thermal width  $\Gamma(T)$  of the  $0^{++}$  glueball begins already far below  $T_c$  in the confinement phase. This may be an attractive feature for the experimental observation of the thermal effect.

#### 3. Comparison of the Breit-Wigner analysis with the pole-mass analysis

Finally, we consider the relations between the pole-mass analysis and the Breit-Wigner analysis. As is mentioned before, the Breit-Wigner analysis is a straightforward extension to the pole-mass analysis. In fact, they coincide in the vanishing width limit  $\Gamma \rightarrow +0$ . In this limit, we have the equality,

$$m_G(T) = \omega_0(T). \quad (55)$$

However, in the presence of the width  $\Gamma$ , the relation between  $m_G(T)$  and  $\omega_0(T)$  becomes nontrivial, and we are left with the inequality,

$$m_G(T) \leq \omega_0(T). \quad (56)$$

To see this, we consider the spectral representation Eq. (5), where the temporal correlator  $G(t)$  is expressed as an average of the hyperbolic cosine of frequency  $\omega$  with the weight as

$$\frac{\rho(\omega)}{2 \sinh(\beta\omega/2)}. \quad (57)$$

Suppose the idealized case where the spectral function  $\rho(\omega)$  is completely dominated by a single peak. In this case, Eq. (57) reads

$$W(\omega) \equiv \frac{2\pi A \left( \delta_\Gamma(\omega - \omega_0) - \delta_\Gamma(\omega + \omega_0) \right)}{2 \sinh(\beta\omega/2)}. \quad (58)$$

To define the pole-mass, we approximate the weight  $W(\omega)$  with the  $\delta$ -functions as

$$\frac{2\pi A \left( \delta(\omega - m_G) + \delta(\omega + m_G) \right)}{2 \sinh(\beta m_G/2)}, \quad (59)$$

where the pole-mass  $m_G$  is determined so as to reproduce the shape of  $G(t)/G(0)$  in a fit range as faithful as possible. Note that  $\sinh(\beta\omega/2)$  in the denominator of Eq. (58) works as a biased factor, which enhances the smaller  $\omega$  region while suppressing the larger  $\omega$  region. As a consequence of this biased factor, the peak position of  $W(\omega)$  is shifted from  $\omega_0$  to a smaller value, which leads to the inequality Eq. (56).

To make a rough estimate of the pole-mass  $m_G$ , we consider the peak position  $\omega = \omega_{\max} (> 0)$  of the weight  $W(\omega)$  in Eq. (58), which is defined as

$$\left. \frac{d}{d\omega} W(\omega) \right|_{\omega=\omega_{\max}} = 0. \quad (60)$$

We adopt the simple identification as

$$m_G \simeq \omega_{\max}. \quad (61)$$

In the confinement phase  $T < T_c$ , the results of the Breit-Wigner fit indicate the inequality as

$$\omega_0 \gg \Gamma, T. \quad (62)$$

In this case, Eq. (58) can be approximated as

$$W(\omega) \simeq 2\pi A e^{-\beta\omega/2} \delta_\Gamma(\omega - \omega_0) \quad (63)$$

in the region of  $\omega \sim \omega_0$ . Hence, Eq. (60) reduces to

$$(\omega_{\max} - \omega_0) + \frac{\beta}{4} \{ (\omega_{\max} - \omega_0)^2 + \Gamma^2 \} \simeq 0. \quad (64)$$

As a consequence of the simple identification in Eq. (61), we find the relation among  $m_G(T)$ ,  $\omega_0(T)$  and  $\Gamma(T)$  as

$$m_G(T) \simeq \omega_0(T) - \left\{ 2T - \sqrt{4T^2 - \Gamma(T)^2} \right\} \leq \omega_0(T), \quad (65)$$

which seems consistent with our numerical results below  $T_c$ .

We make a comment on the experimentally observed particle mass at finite temperature in the presence of the width  $\Gamma$ . In the high-energy experiments, the spectral function  $\rho(\omega)$  is actually observed, providing the relevant information of the mass and the width of the particle at finite temperature. In fact, the experimentally observed

mass is expected to be distributed around  $m = \omega_0(T)$  with the width  $\Gamma(T)$ . As long as the width  $\Gamma$  is enough narrow, the pole-mass  $m_G(T)$  provides a good approximation of the peak position of  $\omega_0(T)$  in  $\rho(\omega)$ . In this case, the pole-mass  $m_G(T)$  can be regarded as the thermal particle mass. In fact, in all of the previous studies of the hadronic temporal correlations [13, 14, 16], the single-cosh analysis has been used assuming that the thermal width is enough narrow. However, when the width  $\Gamma$  becomes wide, the pole-mass  $m_G(T)$  obtained from the single-cosh analysis suffers from the effect of the biased factor “ $\sinh(\beta\omega/2)$ ” in the denominator in Eq. (57). Therefore,  $m_G(T)$  is shifted from  $\omega_0$  to a smaller value. In this case, the Breit-Wigner analysis is preferable. As is demonstrated before, the Breit-Wigner analysis physically means the direct measurement of the pole position of the low-lying particle in the complex  $\omega$ -plane, i.e., the shape of the low-lying peak in the spectral function  $\rho(\omega)$ . It provides the mass and the width of the particle at finite temperature as the center  $\omega_0(T)$  and the width  $\Gamma(T)$ , respectively.

## VI. SUMMARY AND CONCLUDING REMARKS

We have studied the thermal properties of the  $0^{++}$  and  $2^{++}$  glueballs using SU(3) anisotropic lattice QCD with  $\beta_{\text{lat}} = 6.25$ , the renormalized anisotropy  $\xi \equiv a_s/a_t = 4$  ( $a_s \simeq 0.084$  fm and  $a_t \simeq 0.021$  fm) over the lattice of the size  $20^3 \times N_t$  with  $N_t = 24, 26, 28, 30, 33, 34, 35, 36, 37, 38, 40, 43, 45, 50, 72$  at the quenched level.

To begin with, we have measured the temporal correlators  $G(t)$  for the lowest  $0^{++}$  and  $2^{++}$  glueballs using more than 5,500 gauge configurations at each temperature. In this calculation, we have adopted the smearing method to construct the suitable operator for the lowest-lying  $0^{++}$  and  $2^{++}$  glueballs on the lattice. We have also provided an analytical consideration on the physical meaning of the smearing procedure based on the spatial distribution of the gluon field in the smeared operator.

Next, we have performed the pole-mass measurements of the thermal glueballs from  $G(t)$  by adopting the procedure used in the standard hadron mass measurements. For the lowest  $0^{++}$  glueball, we have observed a significant pole-mass reduction of about 300 MeV near  $T_c$  or  $m_G(T \simeq T_c) \simeq 0.8m_G(T \sim 0)$ , while its size remains almost unchanged as  $\rho(T) \simeq 0.4$  fm. This pole-mass shift is actually much larger than any other pole-mass shifts which have been ever observed in the meson sector [13, 14] with the similar analysis in lattice QCD.

Finally, for completeness, we have performed a more general new fit-analysis of the temporal glueball correlator  $G(t)$  as an attempt to take into account the effects of the possible appearance of the thermal width  $\Gamma(T)$  of the bound-state peak. We have proposed the Breit-Wigner form as a generalized fit-function  $g_\Gamma(t)$  for the



lowest-peak in the spectral function  $\rho(\omega)$  of the temporal correlator  $G(t)$  at finite temperature. This ansatz is also applicable to the temporal correlators of various thermal hadrons. In this advanced analysis, we have found a significant broadening of the lowest-gluon peak as  $\Gamma(T) \sim 300$  MeV near  $T_c$  as well as a rather modest reduction in its center of about 100 MeV.

We have investigated also the temporal correlators of the color-singlet modes corresponding to the glueballs in the deconfinement phase. We have found that the thermal width  $\Gamma(T)$  increases monotonically with increasing temperature both in the  $0^{++}$  and the  $2^{++}$  glueball channels. However, from only our lattice data, it is difficult to determine whether such color singlet modes really survive above  $T_c$  or not as a meta stable modes, which is left for the future studies.

In this way, these two analyses have indicated the significant thermal effects to the lowlying thermal  $0^{++}$  glueball near  $T_c$ , such as the considerable pole-mass reduction or the width broadening. Note that the actual decay width of the glueball candidates,  $f_0(1500)$  and  $f_0(1710)$ ,

are known to be about 100 MeV, which is rather small. Hence, either the 300 MeV pole-mass reduction or the thermal width broadening of 300 MeV, if happens, will be seen in the change of the spectral function in the high-energy experiment. Therefore, the thermal properties of glueball may provide an interesting signal of the precritical phenomenon of the QGP creation in the future experiment in RHIC. For more direct comparison with the experiment, it is desirable to include the dynamical-quark effect.

### Acknowledgement

We would like to thank T. Doi for his useful comments. H. S. is supported by Grant for Scientific Research (No.12640274) from Ministry of Education, Culture, Science and Technology, Japan. H. M. is supported by Japan Society for the Promotion of Science for Young Scientists. The lattice QCD Monte Carlo calculations have been performed partly on NEC-SX5 at Osaka University and partly on SR8000 at KEK.

- 
- [1] W. Greiner and A. Schäfer, “Quantum Chromodynamics”, (Springer-Verlag, Berlin, 1994) 1.
- [2] T. Hashimoto, K. Hirose, T. Kanki and O. Miyamura, Phys. Rev. Lett. **57**, 2123 (1986).
- [3] T. Matsui and H. Satz, Phys. Lett. **B178**, 416 (1986).
- [4] G. Boyd, J. Engels, F. Karsch, E. Laermann, C. Legeland, M. Lutgemeier, B. Petersson, Nucl. Phys. **B469**, 419 (1996).
- [5] F. Karsch, E. Laermann and A. Peikert, Nucl. Phys. **B605**, 579 (2001).
- [6] T. Hatsuda and T. Kunihiro, Phys. Rev. Lett. **55**, 158 (1985); Phys. Lett. **B185**, 304 (1987).
- [7] H. Ichie, H. Suganuma and H. Toki, Phys. Rev. **D52**, 2944 (1995).
- [8] CERES Collaboration, Phys. Rev. Lett. **75**, 1272 (1995).
- [9] V.L. Eletsky, B.L. Ioffe, J.I. Kapusta, Eur. Phys. J. **A3**, 381 (1998); Nucl. Phys. **A661**, 514 (1999).
- [10] H. Matsufuru et al., Proc. of *Quantum Chromodynamics and Color Confinement*, edited by H. Suganuma et al. (World Scientific, 2001) 246.
- [11] O. Kaczmarek, F. Karsch, E. Laermann and M. Lutgemeier, Phys. Rev. **D62**, 034021 (2000).
- [12] C. DeTar and J.B. Kogut, Phys. Rev. Lett. **59**, 399 (1987).
- [13] QCD-TARO Collaboration, Phys. Rev. **D63**, 054501 (2001).
- [14] T. Umeda, R. Katayama, O. Miyamura and H. Matsufuru, Int. J. Mod. Phys. **A16**, 2215 (2001).
- [15] N. Ishii, H. Suganuma and H. Matsufuru, Proc. of *Lepton Scattering, Hadrons and QCD*, edited by W. Melnitchouk et al. (World Scientific, 2001) 252.
- [16] N. Ishii, H. Suganuma and H. Matsufuru, Phys. Rev. **D66**, 014507 (2002).
- [17] E. Laermann and P. Schmidt, Eur. Phys. J. **C20**, 541 (2001).
- [18] B. Grossmass, S. Gupta, U. M. Heller and F. Karsch, Nucl. Phys. **B417**, 289 (1994).
- [19] S. Datta and S. Gupta, Nucl. Phys. **B534**, 392 (1998). S. Datta and S. Gupta, Phys. Lett. **B471**, 382 (2000).
- [20] T. R. Klassen, Nucl. Phys. **B533**, 557 (1998).
- [21] C. J. Morningstar and M. Peardon, Phys. Rev. **D60**, 034509 (1999), and references therein.
- [22] J. Sexton, A. Vaccarino and D. Weingarten, Phys. Rev. Lett. **75**, 4563 (1995), and references therein.
- [23] M. J. Teper, OUP-98-88-P (1998), hep-th/9812187.
- [24] K. K. Seth, Nucl. Phys. **A675**, 25c (2000), and references therein.
- [25] I. Montvay and G. Münster, *Quantum Fields on a Lattice*, (Cambridge, 1994) 1.
- [26] H. J. Rothe, *Lattice Gauge Theories*, (World Scientific, 1992) 1.
- [27] T. Hashimoto, A. Nakamura and I. O. Stamatescu, Nucl. Phys. **B400**, 267 (1993).
- [28] APE Collaboration, Phys. Lett. **B192**, 163 (1987).
- [29] T. T. Takahashi, H. Matsufuru, Y. Nemoto and H. Sugauma, Phys. Rev. Lett. **86**, 18 (2001).
- [30] Y. Iwasaki, K. Kanaya, T. Kaneko and T. Yoshié, Phys. Rev. **D56**, 151 (1997).
- [31] P. de Forcrand and K.-F. Liu, Phys. Rev. Lett. **69**, 245 (1992).
- [32] W.-S. Hou, C.-S. Luo, G.-G. Wong, Phys. Rev. **D64**, 014028 (2001).